Combined physical and biogeochemical assessment of mesoscale eddy parameterisations in ocean models: eddy induced advection at non-eddying resolutions

X. Ruan, Damien Couespel, Marina Lévy, J. Li, J. Mak, Y. Wang

Combined physical and biogeochemical assessment of mesoscale eddy parameterisations in ocean models: eddy induced advection at non-eddying resolutions

X. Ruan[a,b,1], D. Couespel[c,d], M. Lévy[d], J. Li[a,b], J. Mak[a,b,1], Y. Wang[a,b]

[a]*Department of Ocean Science, Hong Kong University of Science and Technology*
[b]*Southern Marine Science and Engineering Guangdong Laboratory (Guangzhou)*
[c]*NORCE Norwegian Research Centre, Bjerknes Centre for Climate Research*
[d]*Sorbonne Université, LOCEAN-IPSL, CNRS/IRD/MNHN*

Abstract

Ocean components of Earth System Models employed for climate projections do not routinely resolve mesoscale eddies for computational cost reasons, and the associated subgrid processes are still parameterised. While the performance of physics parameterisations in a numerical ocean model is normally assessed by examining the associated physical responses, biogeochemical responses are also important but often treated separately. Given recent advances in mesoscale eddy parameterisations, specifically for the eddy induced advection, this work systematically explores the joint consequences for physical as well as biogeochemical responses brought about by a more updated proposal for the eddy induced velocity coefficient, in the context of an idealised ocean relevant model. Relative to a high resolution mesoscale eddy resolving model, the more updated mesoscale eddy parameterisation is able to capture aspects of the model truth in the physical responses. The biogeochemistry response is however rather more subtle, where a 'better' response with the conventional eddy parameterisation with a constant coefficient could arise from a physically inconsistent response, while a parameterisation that improves the bulk physical response may still fall short in its biogeochemical response. The present work highlights a need to assess both physical and biogeochemical aspects when judging the performance of eddy parameterisations, and additionally provides some important baseline model sensitivities that future assessments employing other parameterisations or in more complex settings could compare against.

Keywords: mesoscale eddy parameterisation, numerical modelling, climate change, biophysical interactions

1. Introduction

The ocean circulation plays a crucial role in the Earth system's heat, carbon and nutrient cycles, and affects the global climate and the marine ecosystem (e.g. Rahmstorf, 2002; Doney et al., 2012). Over the decadal to centennial time-scales, more heat is expected to reside in the upper part of the ocean under climate projection exercises (e.g, IPCC, 2019), strengthening the upper ocean stratification and changing the ocean ventilation pathways (e.g., Bindoff and McDougall, 1994; Li et al., 2020). The ocean meridional overturning circulation is projected to slow down, partly via the shoaling of the pycnocline, though uncertainties still exist (e.g., Bellomo et al., 2021). Changes in the ocean overturning circulation can affect the bulk transport of nutrients, which can then have large-scale impacts on the phytoplankton populations. As primary producers, phytoplankton play an important role in the global carbon cycle and impact issues of food security via their position at the base of most oceanic food webs. While there is large uncertainty in the physiological responses of various marine biomass to the changing marine environment in terms of heat stress, nutrient abundance, acidity and others (e.g., Kwiatkowski et al., 2020; Tagliabue et al., 2021; Martiny

Email addresses: xruanaa@connect.ust.hk (X. Ruan), julian.c.l.mak@googlemail.com (J. Mak)
[1]Corresponding authors.

et al., 2022), it is not controversial to say that the physical circulation can impact the broad regional and global biogeochemical response. One such link is the impact of the circulation on nutrient supply, though such projections often come with large uncertainties given the nonlinear interactions present in the complex Earth system (e.g., Lotze et al., 2019).

Earth System Models are invaluable tools for probing and constraining the physical and biogeochemical responses in the marine system to the changing environment. These numerical models simulate the evolution of the Earth system components and their interactions (e.g., Bonan and Doney, 2018; Séférian et al., 2019; Lee et al., 2022), with the assumption that the processes implemented into the numerical models are correct. However, even with the increasing computational power available, present state-of-the-art Earth System Models still mostly utilise ocean components at approximately 1° horizontal resolution that do not explicitly permit geostrophic mesoscale eddies (e.g., Hewitt et al., 2020, 2022). Geostrophic mesoscale eddies play a crucial role in regulating the ocean circulation responses, which not only have local effects, but also impact the larger scale regional and global mean state (e.g. Lévy et al., 2012). Although there is an increasing push for ocean models to be mesoscale eddy resolving (Fox-Kemper et al., 2019; Kwiatkowski et al., 2020; Hewitt et al., 2022) or at least eddy rich (at around $1/12°$ horizontal resolutions, Hallberg, 2013), models at such resolutions remain computationally prohibitive, and global Earth System Models with an ocean component at the mesoscale eddy permitting regime at around $1/4°$ horizontal resolution is a more realistic target (Hewitt et al., 2017, 2020, 2022; Roberts et al., 2020). Given the physical influence on the biogeochemical response and the anticipated developments of ocean models over the next decade, there is a need to probe, constrain and understand the sensitivities of the physical and biogeochemical responses in ocean models at the non-eddy resolving, eddy permitting as well as the eddy rich/resolving resolutions.

For those models that do not explicitly permit mesoscale eddies, parameterisations are often employed to mimic the feedback of geostrophic mesoscale eddies. Often employed are what we would term here as *diffusive* closures, such as isoneutral diffusion (e.g., Redi, 1982; Griffies, 1998) and the Gent–McWilliams (GM) scheme (Gent and McWilliams, 1990; Gent et al., 1995). Isoneutral diffusion leads to tracer diffusion along the isoneutral directions, while the GM scheme leads to an eddy induced advection of tracers that flattens isoneutral slopes, and both are consistent with the adiabatic nature of mesoscale eddies generated by baroclinic instabilities (e.g., Vallis, 2006). Such diffusive closures were designed for coarse resolution models with no explicitly resolved eddies, considered more standard, and variants of such schemes exist in most numerical ocean models (e.g. MITgcm, Marshall et al. 1997a,b; NEMO, Madec 2008; FESOM, Wang et al. 2014; MOM, Adcroft et al. 2019). On the other hand, mesoscale eddies can also lead to sharpening of large-scale jets (via inverse cascades, eddy induced momentum convergence, or otherwise, e.g. Waterman and Jayne, 2012; Waterman and Hoskins, 2013), which is increasingly modelled by *backscatter* based parameterisations (e.g., Bachman, 2019; Jansen et al., 2019). Recent advances in both classes of parameterisations have led to lower resolution models that are more in line with the eddy rich/resolving models at least in the physical response. Advances in diffusive schemes tend to focus more on coarse resolution models, some of which have led to improvements in sensitivities of the circulation to changing forcing scenarios (e.g., Farneti et al., 2015; Mak et al., 2018, 2022b). Backscatter schemes have received more attention in eddy permitting models because of their ability to strengthen the represented eddy energy levels and ocean currents (e.g., Bachman, 2019; Jansen et al., 2019).

The biogeochemical response to such recent updates in physics parameterisations have been, on the other hand, lackingwhen it is known that model represented physics can have a very substantial impact on the resulting physical and/or biogeochemical metrics of interest. Modifying the represented eddy-mean feedbacks can have a significant effect on the ventilation rate and pathways, affecting the represented ocean heat content (e.g., de Boer et al., 2007; Zhang and Vallis, 2013; Zanna et al., 2019b; Mak et al., 2022b; Newsom et al., 2022), carbon (England and Rahmstorf, 1999; Gnanadesikan et al., 2015; Khwatiwala et al., 2018), oxygen (Matear et al., 2000; Helm et al., 2011; Bopp et al., 2017; Takano et al., 2018), and nutrient distributions (Lévy et al., 1999; Tschumi et al., 2011; Bopp et al., 2013; Couespel et al., 2021). With the prevalent use of numerical ocean general circulation models for probing and predicting biophysical interactions (e.g., Bopp et al., 2013; Berthet et al., 2019; Swearer et al., 2019; Séférian et al., 2019), it is important to investigate how the physics parameterisations (*i*) modify the modelled physical states, and (*ii*) affect the biogeochemical responses. Such an investigation is required since there is no guarantee that improvements in physical processes necessarily lead to a 'better' biogeochemical response, given the nonlinear interactions inherent in a complex system.

Global and/or realistic models, while useful for making predictions and informing policies (e.g., IPBES, 2019), are computationally expensive and possess a large number of degrees of freedom, making it difficult to attribute the various

causalities. While ultimately these realistic and complex Earth System Models should be used when quantitatively assessing the impacts of eddy parameterisations, for delineating the causality and interactions between the physical parameterisations and the resulting physical and biogeochemical responses, we consider here a complementary approach by utilising idealised numerical models, focusing on the qualitative differences arising from the choice of eddy parameterisations. We focus on a systematic assessment of mesoscale eddy parameterisations and their qualitative impact on the nutrient stream or relay, and their subsequent impact on Net Primary Production (NPP) (e.g., Williams et al., 2017, 2011; Whitt and Jansen, 2020; Gupta et al., 2022). We employ a double gyre setting with a simple biogeochemistry model, with prescribed atmospheric forcing and an idealised climate change scenario (Couespel et al., 2021). The double gyre setting has the benefit that the model behaviours and limitations are relatively well-known (e.g., Jackson et al., 2006; Lévy et al., 2010, 2012, 2014; Stewart et al., 2021), and the high resolution eddy resolving 'model truths' are more computationally accessible because of the limited spatial extent.

Even with the reduced complexity afforded by the choice of numerical model, there are multiple parameterisations for mesoscale turbulence. Here we focus on diffusive eddy closures, specifically on the GM-based parameterisations for the eddy induced advection; an analogous investigation into the effects of isoneutral diffusion, backscatter type eddy parameterisations, and extensions into the eddy permitting models will be reported in subsequent publications. The models to be investigated here are non-eddy resolving, differing by the GM-type closures they employ, and the qualitative performance of these will be judged against the high resolution eddy resolving model truths. The GM parameterisation variants and the numerical model set up are described in §2. In §3 we report the qualitative differences in both the physical and biogeochemical responses arising from the choice of closures. In §4 we subject the models to idealised climate change scenarios to investigate analogous model sensitivities. The article concludes in §5, critically evaluating the advantages and shortfalls provided by the choices of GM-based closures.

2. Mesoscale eddy parameterisations and numerical set up

Two canonical types of diffusive closures associated with geostrophic turbulence are those based on isoneutral diffusion (e.g., Redi, 1982) and the Gent–McWilliams scheme (GM, Gent and McWilliams, 1990). The former refers to diffusion of tracers along the isoneutral direction, while the latter is an eddy induced advection (e.g., Gent et al., 1995; Treguier et al., 1997; Griffies, 1998) although it resembles a horizontal buoyancy diffusion (in the quasi-geostrophic limit, e.g. Treguier et al., 1997) or a layer thickness diffusion (e.g., Gent and McWilliams, 1990). The isoneutral diffusion and GM schemes are both known to affect the physical and biogeochemical response. Isoneutral diffusion modifies the rate of tracer ventilation, and the GM schemes affect the structure of the tracer ventilation through its impact on the density stratification. Relatively speaking, there are more studies on assessing GM-based schemes (e.g., Visbeck et al., 1997; Eden and Greatbatch, 2008; Cessi, 2008; Hofman and Morales Maqueda, 2011; Munday et al., 2013; Zhang and Vallis, 2013; Bates et al., 2014; Farneti et al., 2015; Mak et al., 2018, 2022b), although there have also been increasing interest in isoneutral diffusion, assessing its impact as well as improving on the standard implementation with constant diffusivity (e.g., Ferrari and Nikurashin, 2010; Pradal and Gnanadesikan, 2014; Jones and Abernathey, 2019, 2021; Groeskamp et al., 2021; Holmes et al., 2022; Chouksey et al., 2022). While both processes are related to mesoscale turbulence, and there are works that suggest relationships between the two (e.g., Smith and Marshall, 2009; Abernathey et al., 2013), owing to the larger interest in GM-based closures, in this work we focus primarily on the consequences afforded by different GM-based schemes, and consider a prescribed constant isoneutral diffusivity κ_{iso}. The model sensitivity to κ_{iso} by itself was found to be rather mild in the present model, although nonlinear feedback loops can be present, suggesting that further investigation is required in this area; see Appendix A for details.

2.1. GM-based parameterisations

The GM-scheme introduces an eddy induced velocity $\mathbf{u}^*$ to the tracer advection equation (e.g., Griffies, 1998; Ferreira et al., 2005):

$$\mathbf{u}^* = -\nabla \times (\kappa_{\mathrm{gm}} \boldsymbol{s}). \tag{1}$$

Here, $\boldsymbol{s} = -\nabla_H \rho / N^2$ the isopycnal slope in the horizontal directions, ∇_H the horizontal gradient operator, $N^2 \sim -\partial\rho/\partial z$ the vertical buoyancy gradients associated with the resolved state, ρ denotes the dynamically relevant density, and κ_{gm} will be termed the GM-coefficient in this work. The GM scheme is widely used because of its inherent properties,

such as adiabatic advection leading to slumping of isopycnals, positive-definite generation of eddy energy and layer-wise conservation of moments (e.g., Gent et al., 1995), as well as numerical advantages (numerical stability due to the slumping action, reduction of unrealistic deep convection; e.g., Danabasoglu et al. 1994). A choice often utilised in idealised models takes the simple prescription of

$$\kappa_{\rm gm} = \kappa_0 = \text{constant}. \tag{2}$$

2.1.1. GEOMETRIC

As it is desirable to maintain the properties afforded by the GM scheme even if one does not believe a simple prescription of $\kappa_{\rm gm}$ = constant will suffice, a prevalent research focus has been on improving on the functional form of $\kappa_{\rm gm}$ (e.g., Visbeck et al., 1997; Treguier et al., 1997; Ferreira et al., 2005; Cessi, 2008; Eden and Greatbatch, 2008; Hofman and Morales Maqueda, 2011; Marshall et al., 2012; Jansen et al., 2015, 2019). We consider here on a form of the GM scheme arising from the GEOMETRIC framework for analysing eddy-mean flow interactions (see Marshall et al., 2012; Maddison and Marshall, 2013). In the present form, analysis within the GEOMETRIC framework suggests scaling $\kappa_{\rm gm}$ as (Mak et al., 2018, 2022b)

$$\kappa_{\rm gm} = \alpha \frac{\int E \, {\rm d}z}{\int (M^2/N) \, {\rm d}z}, \tag{3}$$

where $M^2 \sim |\nabla_H \rho|$ denotes the horizontal buoyancy gradients associated with the resolved state, α is a non-dimensional tuning parameter (bounded in magnitude by one), E is the total (potential and kinetic) eddy energy, and the resulting $\kappa_{\rm gm}$ varies in time and in the horizontal (but is depth-independent with the present specification). Unlike most other existing proposals for the $\kappa_{\rm gm}$ that utilise mixing length type arguments with dependence on the eddy kinetic energy, the GM-version of GEOMETRIC arises from a mathematically rigorous bound that results from analysing the Eliassen–Palm flux tensor that encodes the eddy-mean feedbacks (Marshall et al., 2012; Maddison and Marshall, 2013). The bound results in a linear dependence on the total eddy energy E (compared to mixing length based parameterisations with a square root scaling; e.g., Eden and Greatbatch 2008; Jansen et al. 2015, 2019), which leads to a more significant state-dependent response. Notably, out of the GM-based parameterisations, the GM-version of GEOMETRIC has more evidence in support of its use, from a diagnostic point of view (Bachman et al., 2017; Wang and Stewart, 2020; Wei et al., 2022), and prognostic calculations in idealised models (Mak et al., 2017, 2018) as well as in realistic models (Mak et al., 2022b). In particular, the GM-version of GEOMETRIC in the aforementioned prognostic calculations have been shown to lead to improved sensitivities of the modelled ocean circulation to changes in forcing over the standard prescriptions of the $\kappa_{\rm gm}$, notably in the Antarctic Circumpolar Current transport and the global Meridional Overturning Circulation strength.

In a prognostic calculation with a coarse resolution model, E is provided using a depth-integrated eddy energy budget. Denoting (x, y) to be the zonal and meridional directions respectively, following Mak et al. (2022b), the eddy energy budget used with GEOMETRIC is given by

$$\frac{\rm d}{{\rm d}t}\int E \, {\rm d}z + \underbrace{\nabla_H \cdot \left((\widetilde{\mathbf{u}}^z - |c| \, \mathbf{e}_x) \int E \, {\rm d}z \right)}_{\text{advection}} = \underbrace{\int \kappa_{\rm gm} \frac{M^4}{N^2} \, {\rm d}z}_{\text{source}} - \underbrace{\lambda \int (E - E_0) \, {\rm d}z}_{\text{dissipation}} + \underbrace{\eta_E \nabla_H^2 \int E \, {\rm d}z}_{\text{diffusion}}, \tag{4}$$

where the depth-integrated eddy energy is advected by the depth average flow $\widetilde{\mathbf{u}}^z$ with westward propagation at the long Rossby wave phase speed $|c|$ (e.g., Chelton et al., 2011; Klocker and Marshall, 2014). The growth of eddy energy comes from the slumping of mean density surfaces, and diffused in the horizontal (Grooms, 2015; Ni et al., 2020a,b) with η_E denoting the associated eddy energy diffusivity. A linear dissipation of eddy energy at rate λ (but maintaining a minimum eddy energy level E_0) is utilized, so λ^{-1} is an eddy energy dissipation time-scale, which is a bulk parameterisation of energy fluxes out of the mesoscales resulting from numerous dynamical processes (e.g., Mak et al., 2022a).

In this work we focus on a comparison between calculations employing the GM-version of the GEOMETRIC parameterisation (denoted GEOM), to be compared with the calculations employing a prescribed constant $\kappa_{\rm gm}$ (denoted CONST); we have also performed calculations with simpler proposals of $\kappa_{\rm gm}$ that are state dependent

(Treguier et al. 1997; cf. Visbeck et al. 1997), and will comment on the results from those calculations where appropriate. Although we have not performed calculations employing other existing energetically constrained proposals (e.g., $\kappa_{\rm gm} \sim \sqrt{K}$ of Jansen et al., 2019, where K is the eddy kinetic energy), we speculate in the discussion section the expected responses given the results from in the present work.

2.2. Model set up

Our main focus is to systematically assess the qualitative differences arising from different eddy parameterisation variants, and for this purpose an idealised numerical ocean model is employed. A double gyre model based on the set up of Couespel et al. (2021) using the Nucleus for European Modelling of the Ocean (NEMO; Madec 2008) was used. The gyre model here is a "straightened" version of the standard gyre configuration test case that comes with NEMO. The model is already coupled to an idealised biogeochemistry model within NEMO (cf. Lévy et al., 2010, 2012) and has been used to study both physical and biogeochemical responses in the aforementioned work. To recap, the domain is square with sides of length 3180 km and depth 4 km, formulated on a β-plane with the Southern boundary at 20° N, extending to the Northern boundary at 50° N. The domain has no bathymetry, and is bounded by vertical walls that are aligned with longitudes and latitudes on all sides. While the presence of bathymetry is known to have impacts on the large-scale circulation (e.g., Jackson et al., 2006; Gula et al., 2015; Stewart et al., 2021), there is the added subtlety on how one should parameterise eddy feedbacks over slope regions (e.g., Wang and Stewart, 2020; Wei et al., 2022). For simplicity and to reduce the degrees of freedom in the problem, we opted for the flat bottom case. We employ a non-linear bottom drag, and impose free-slip conditions on the lateral boundaries. The model utilises a linear equation of state with temperature and salinity, and vertical mixing is via a turbulent kinetic energy scheme (Gaspar et al., 1990). Atmospheric forcing is through the flux formulation, and the forcings (wind stress, penetrative solar radiation, pseudo-atmospheric temperature Θ^* for computing sea surface temperature restoring, freshwater flux) are all zonally symmetric and with a prescribed repeating seasonal cycle and no period beyond a year, and there is no net salinity flux (see Lévy et al., 2010, Fig.1).

The model employs an idealised biogeochemistry model LOBSTER (see e.g., Lévy et al., 2012) with standard reference settings, and with eddy induced advective and diffusive contributions from the GM-based and Redi schemes respectively. The LOBSTER model uses nitrogen as the currency, and the six biogeochemical variables are concentrations of detritus, zooplankton, phytoplankton, nitrate, ammonium, and dissolved organic matter; variables of particular interest to the work here are phytoplankton and nitrate for their links to Net Primary Production (NPP). As LOBSTER does not represent physiological changes with changes in temperature, changes observed are solely due to changes in the transport of the biogeochemical tracers, providing a better focus on the large-scale links between physics and biogeochemistry.

The differences between the model employed in this work to that of Couespel et al. (2021) are the following:

- version of NEMO (NEMO v4.0.5 r14538 instead of v3.4 r4826),
- a slightly different initialisation of nitrate concentration at the start of the perturbation experiments (no averaging of the deep ocean nitrate concentration),
- the model truth is taken here to have a horizontal resolution of $1/12°$ instead of $1/9°$.

The updated version of NEMO already has the GM-version of GEOMETRIC implemented from the work of Mak et al. (2022b), and it was easier to adapt the model configuration to the newer NEMO than to write the GEOMETRIC parameterisation into an older version of NEMO. Sample calculations show that the different initialisation of the nitrate concentration at the deeper ocean have no impact on the conclusions in this article. The horizontal resolution of the model truth was increased to $1/12°$ partly as a balance to resolve mesoscale processes, but without resolving too much of the submesoscale processes, so that there is a more suitable comparison between the model truth and the coarse resolution models employing the GM-based schemes, since the GM-based schemes are not designed to capture submesoscale processes. The model truth horizontal resolution of $1/12°$ was also chosen for the suggestive analogy with the global NEMO ORCA0083 (also known as ORCA12) configuration that is at a nominal horizontal resolution of $1/12°$, and provides a benchmark reference for our future investigations into eddy permitting models. All the major conclusions of Couespel et al. (2021) are found to hold even with the present changes. A summary of key model parameters is given in Table 1, partly informed by previous works (Couespel et al., 2021; Mak et al., 2022b,a). A brief description of model sensitivities to some of these choices are given in Appendix A.

	R1 (CONST and GEOM)	R12
horizontal resolution	106 km	8.83 km
time step	30 mins	10 mins
momentum diffusion	horizontal ∇^2, $\nu = 10^5$ m^2 s^{-1}	horizontal ∇^4, $\nu = -3 \times 10^{10}$ m^4 s^{-1}
tracer advection	FCT scheme	MUSCL scheme
tracer diffusion	isopycnal ∇^2, $\kappa_{\rm iso} = 10^3$ m^2 s^{-1}	iso-level ∇^4, $\kappa = -10^9$ m^4 s^{-1}
eddy induced advection	CONST ($\kappa_{\rm gm} = 1000$ m^2 s^{-1})	—
	GEOM ($\alpha = 0.04$, $\lambda^{-1} = 135$ days)	—

Table 1: Key model parameter differences between the calculations considered in this work.

2.3. Experimental set up

Following the strategy of Couespel et al. (2021), the physical and biogeochemical model at the 1° resolution starts from model year −2300, spun up over 2000 model years to model year −300 using the CONST variant with constant $\kappa_{\rm gm}$. At model year −300, perturbation experiments were carried out for another 300 years to model year 0 (which is longer than the 100 years considered in Couespel et al. 2021). For the 1° models, the perturbation experiments are with CONST and GEOM. For the 1/12° model R12, the fields are simply interpolated from the 1° model onto the analogous 1/12° grid

Two sets of experiments are performed in this work. A control pre-industrial setting (tagged with a suffix CTL) integrates the aforementioned calculations for another 70 years from model year 0, subject to the same idealised atmospheric forcing. An idealised climate change scenario (tagged with a suffix CC) has the models exposed to the aforementioned idealised seasonal cycle from model year 0, but the atmospheric temperature is given an increasing linear trend of +0.04 °C yr^{-1} over 70 model years, following Couespel et al. (2021) to mimic the SSP5-8.5 scenario (e.g., Tokarska et al., 2020). Fig. 1 shows some of the summary statistics of the spinup and the adjustment under the control and idealised climate change scenario, indicating that a quasi-equilibrium has been reached at least in the upper parts of the ocean (depths less than 700 m) in the perturbation calculations during the spinup stage. Under the idealised climate change scenario, the ocean temperature increases, leading to a stronger stratification (primarily in the upper ocean; not shown) that inhibits nutrient supply and a decrease in NPP across the set of calculations, consistent with the results of Couespel et al. (2021) (see their Fig. 1*d* and A1).

In each of the two sets of experiments we evaluate the performance of the eddy parameterisations by examining both the physical and biogeochemical responses, critically comparing the similarities and differences between GEOM, CONST and the R12 model truth, under the CTL and CC scenario. A working hypothesis is that the physical and biogeochemical responses are improved in the GEOM calculations when compared to the CONST calculations. For evaluating the performance, we consider diagnostics calculated from data time averaged over the analysis period, taken to be the last five years of the calculation (between the start of model year 66 and the end of model year 70). Time averaged quantities are denoted by an overbar

$$\overline{(\cdot)} = \frac{1}{t_1 - t_0} \int_{t_0}^{t_1} (\cdot)\, \mathrm{d}t, \tag{5}$$

with $t_{0,1}$ being start and end of model years 66 and 70 respectively. Following the work of Couespel et al. (2021), our focus is on the responses particularly within the subpolar gyre region, which is the area that is most bioactive in the present setup. We employ the same pre-defined box utilised in Couespel et al. (2021) for our analysis, defined as the area bounded between $y = 35°$ N, 45° N and $z = -700$ m, with the boundaries marked on by the black dashed lines in the subsequent figures where appropriate. The eventual supporting evidence suggests the hypothesis is largely true (see Table 2 in §5), but there are important subtle details to be elaborated on.

Models can display multiple equilibria and/or be affected by internal modes of variability (e.g., Sérazin et al., 2017; Zanna et al., 2019a), where diagnostics would vary depending on the period of analysis. In the present model we considered ensemble experiments perturbing the initial conditions, and we found no significant internal variability beyond inter-annual periods. This could be because of the idealised model as well as the choice of forcing, which has a repeating seasonal cycle and no mode of variability longer than a year. While there is seasonable variability

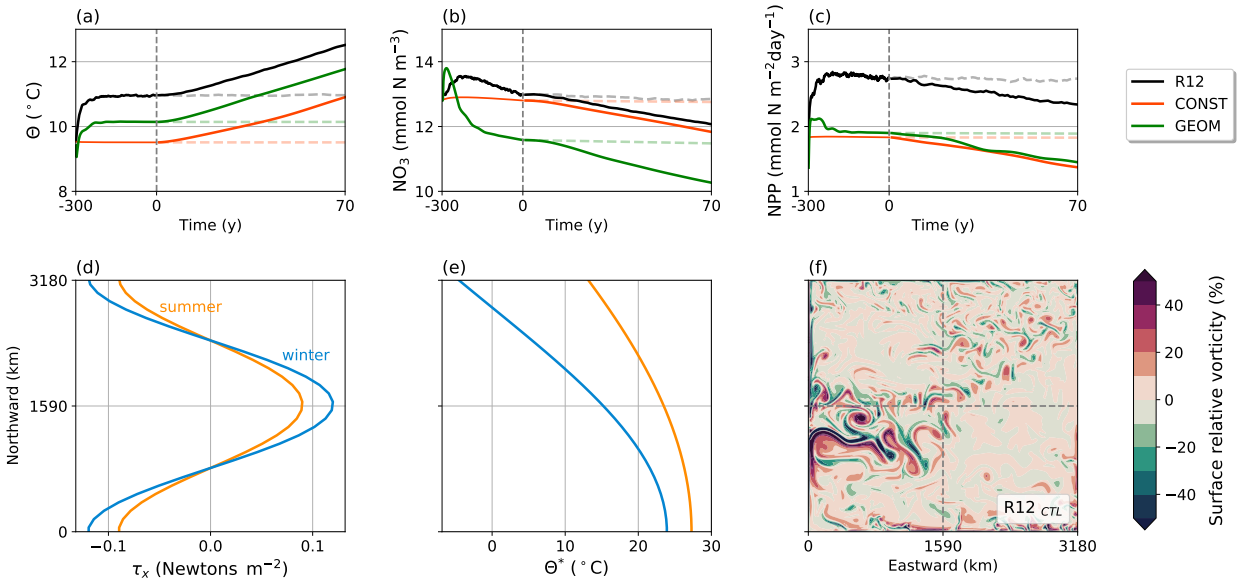

Figure 1: (Top row) Time series of various quantities from the 300-year spin-up (i.e., model years −300 to 0 years) and the experimental period (0 to 70 years), for the model truth (R12, black line) and coarse resolution calculations (CONST, red line; GEOM, green line) for the pre-industrial control scenario (CTL, faint dashed line) and the climate change scenario (CC, solid lines). The time axes are linear in the spinup and analysis period individually. (*a*) Averaged ocean temperature Θ (°C) over the top 700 m of the model domain. (*b*) Model nitrate concentration (NO3, mmol N m^{-3}, where N is the nitrogen currency unit) over the top 700 m of the model domain. (*c*) Domain integrated Net Primary Production (NPP, mmol N m^{-2} day). Shown also are (*d*) the idealised purely zonal wind stress forcing τ_x (Newtons m^{-2}) with seasonal cycle limits, (*e*) the pseudo-atmospheric temperature Θ^* (°C) with seasonal cycle limits, and (*f*) a snapshot of the surface relative vorticity of the model truth R12 (units of the planetary vorticity $f_0 = 2\Omega \sin(20°)$, where Ω is the planetary rotation rate, and 20° is the southern edge of the domain).

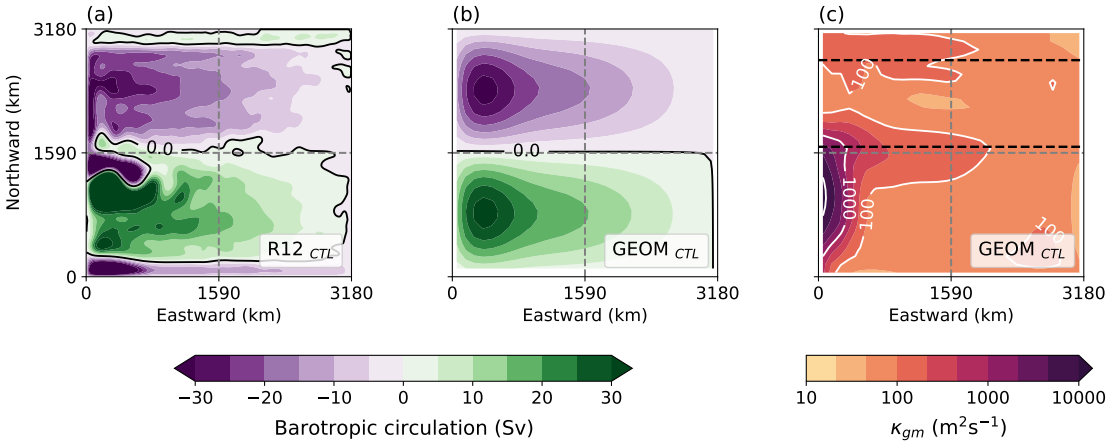

Figure 2: The barotropic streamfunction Ψ_{baro} (in Sv = 10^6 m^3 s^{-1}) of (*a*) R12 and (*b*) GEOM, with the zero contour overlaid as a black line; CONST visually looks identical to GEOM, and has been omitted. Panel (*c*) shows the resulting κ_{gm} distribution from GEOM with the choice of parameters in Table 1; the area enclosed by black dashed lines denote the boundaries of the subpolar gyre box mentioned in text.

particularly in the eddy resolving calculations (cf., Lévy et al., 2014), we are interested in broad scale and long time changes, and the inter-annual variability is averaged out with a multi-year average from our diagnostics. As such, the conclusions drawn from our diagnostics here should thus be regarded as statistically significant. However, we should stress again that we focus on the qualitative rather than the quantitative differences. The primary interest is to see if one parameterisation scheme performs 'better', and less on *how much* better; the latter is more sensitive to context and should be quantified using more realistic models.

3. Comparison of pre-industrial controls

3.1. Physical responses

Fig. 2(a, b) shows the barotropic streamfunction (where the tilde denotes a dummy integration variable)

$$\Psi_{\text{baro}}(x, y) = \int_{-H}^{0} \int_{0}^{x} \overline{v}(\tilde{x}, y, z)\, \mathrm{d}\tilde{x}\, \mathrm{d}z \tag{6}$$

for the R12 and GEOM calculation; the CONST one has been omitted since visually it is indistinguishable from the GEOM one. Both models display the familiar northern hemisphere double gyre pattern with a subtropical gyre to the south and a subpolar gyre to the north. In the R12 calculation, because of eddy rectification effects, the modelled Western Boundary Current is more variable and stronger through eddies converging momentum into the jet extension (e.g., Lévy et al., 2010; Waterman et al., 2011; Waterman and Lilly, 2015). The Western Boundary Current is also slightly south of the latitudinal center line, even though the zonal wind stress is symmetric about the same center line (cf. Lévy et al., 2010). In addition, relatively strong re-circulation regions exist near the northern and southern boundaries as Fofonoff gyres (e.g., Berloff, 2005; Marshall and Adcroft, 2010). All such features are absent in the coarse resolution non-eddying models relying on the standard diffusive mesoscale parameterisations.

In Fig. 2(c) we show the resulting $\kappa_{\text{gm}}(x, y)$ from GEOM. Note that κ_{gm} is large (on the order of a few thousand m^2 s^{-1}) on the Western Boundary Current in the subtropical gyre. The much smaller values of κ_{gm} within the subpolar gyre and particularly its values near the northern boundary will be discussed later. The resulting domain-averaged value of κ_{gm} is about 300 m^2 s^{-1}, and we note the gyre models studied here using such a small value of κ_{gm} everywhere leads to un-physical deep convection particularly along the Western Boundary Current (not shown; cf. Danabasoglu et al., 1994). One benefit then with parameterisation schemes that allow spatial variations of κ_{gm} is that κ_{gm} can be large only where it needs to be large, and this point will be revisited throughout the article.

The concentrated signal of κ_{gm} on the Western Boundary observed in Fig. 2(c) is also consistent with the fact that the represented Western Boundary Current in a coarse resolution model is rather weak, which suggests that the

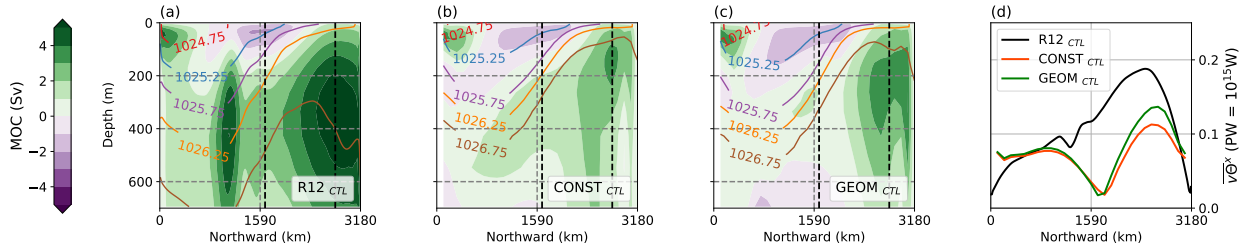

Figure 3: The diagnosed Meridional Overturning Circulation streamfunction Ψ_{MOC} from the model (shading, in Sv = 10^6 m^3 s^{-1}) and lines of constant potential density referenced to sea level (contours, in kg m^{-3}), for (*a*) R12, (*b*) CONST, and (*c*) for GEOM. Panel (*d*) shows the diagnosed northward heat transport (in units of PW = 10^{15} W) for all three cases. The area enclosed by black dashed lines denote the boundaries of the subpolar gyre box mentioned in text.

resulting Meridional Overturning Circulation in the system is also rather weak. In Fig. 3 we show metrics relating to the overturning circulation, namely the diagnosed Meridional Overturning Circulation streamfunction

$$\Psi_{\mathrm{MOC}}(y,z) = \int_{-H}^{z}\int_{0}^{L_x} \overline{v}(x,y,\tilde{z})\,\mathrm{d}x\,\mathrm{d}\tilde{z} \tag{7}$$

between different calculations, some sample isopycnals using potential density referenced to sea level, as well as the diagnosed depth integrated and zonal-mean northward heat transport $\overline{v\Theta}^x$. As shown in Fig. 3, the coarse resolution models CONST and GEOM in general have a weaker overturning strength, partially because of a weaker modelled Western Boundary Current arising from the more diffuse nature of the model. The particularly weak overturning in the subtropical region of the coarse resolution models compared to the R12 model truth is consistent with a weak Western Boundary Current, related to the structure of the displayed isopycnals via thermal wind shear relation. The weaker overturning is reflected in the reduced northward transport of heat. The use of GEOMETRIC provides mild improvements to the represented overturning strength particularly in the subpolar gyre, where the diagnosed Ψ_{MOC} in GEOM is stronger than that in CONST and closer to R12 (area-weighted average root-mean-square mismatch to R12 of 1.99 Sv in GEOM compared to 2.29 Sv in CONST within the subpolar gyre box). The stronger MOC coincides with a larger heat transport (area-weighted average heat transport of 0.094 PW in GEOM compared to 0.078 PW in CONST, calculated from north of 35° N). This increased overturning strength is expected to have a positive effect on the modelled biogeochemical response in the GEOM calculation, as we can expect increased nutrient transport into the subpolar gyre by the nutrient stream or relay (e.g., Williams et al., 2017, 2011; Whitt and Jansen, 2020; Gupta et al., 2022).

The double gyre model here is configured such that the downwelling is most prominent in the northern part of the domain since this region is exposed to the coolest atmospheric temperatures, as seen in the maximum mixed layer depths shown in Fig. 4(*a*-*c*) (diagnosed as the first depth below which $|\sigma_\theta(z) - \sigma_\theta(z = -10\ \mathrm{m})| > 0.01$, where σ_θ is the potential density referenced to sea level). The biggest differences between the calculations are at the northern part of the domain, particularly in the northwestern corner of the domain. Fig. 4(*d*-*f*) shows the histogram of the diagnosed mixed layer north of the subpolar region, where we see CONST has a notable skew towards shallower mixed layer depths relative to GEOM and R12 (in terms of median and distribution). The more shallow mixed layer depths observed in the CONST calculation are consistent with the decrease in the overturning strength, since the mixed layer is correlated to the depths of deep water extent and overturning circulation. One rationalisation is that the GM scheme flattens isopycnals and works against the steepening of isopycnals associated with deep water formation and subsequent convective events. The CONST calculation employs a higher κ_{gm} value in the northern boundary region compared with the resulting κ_{gm} in the GEOM calculation (see Fig. 2*c*), leading to a shallow bias compared to GEOM. The causality highlights the importance of the magnitude and distribution of κ_{gm} in the modelled physical mean state of coarse resolution models, where the mean transport pathways and strengths are being influenced by the explicit or parameterised small-scale feedbacks.

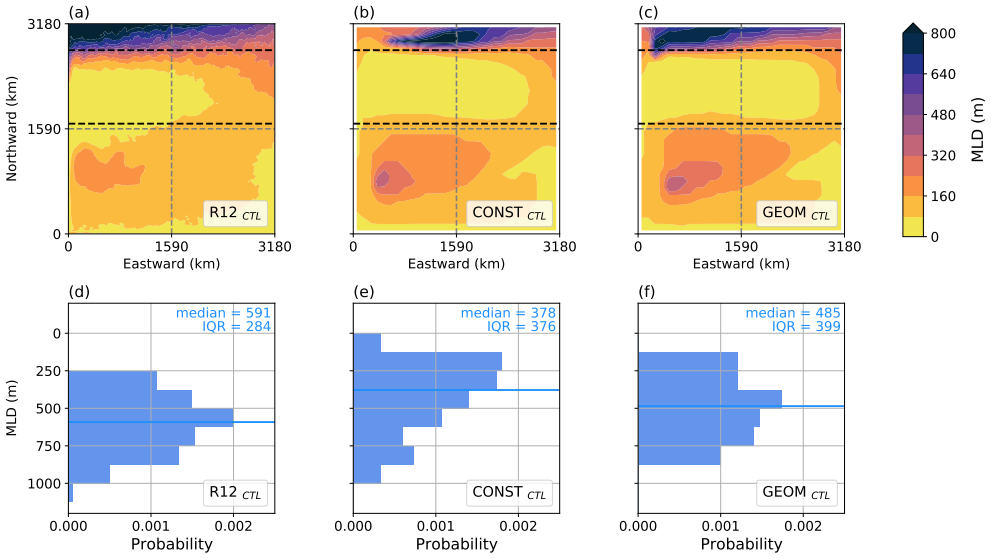

Figure 4: (Top row) Maximum mixed layer depth (m, diagnosed as the first depth below which $|\sigma_\theta(z) - \sigma_\theta(z = -10\text{ m})| > 0.01$, where σ_θ is the potential density referenced to sea level), for (*a*) R12, (*b*) CONST and (*c*) GEOM. The area enclosed by black dashed lines denote the boundaries of the subpolar gyre box mentioned in text. (Bottom row) histogram of mixed layer depth distributions and median (marked on as a line) north of the subpolar gyre region, for (*d*) R12, (*e*) CONST and (*f*) GEOM; the axes of the histograms have been swapped to enable ease of visual comparison.

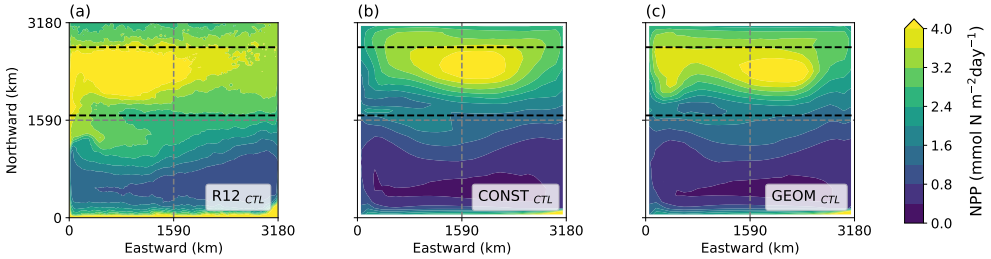

Figure 5: Vertically integrated Net Primary Production (NPP, mmol N m^{-2} day^{-1}, where N is the nitrogen currency) for (*a*) R12, (*b*) CONST and (*c*) GEOM. The area enclosed by black dashed lines denote the boundaries of the subpolar gyre box mentioned in text.

3.2. Biogeochemical responses

Since the CONST calculation is expected to have a weaker circulation (Fig. 3) and shallower mixed layer depths (Fig. 4) relative to the GEOM case, we can expect that GEOM offers some improvements over CONST in the biogeochemical response via changes in the nutrient transport. Fig. 5 shows the horizontal distribution of vertically integrated NPP. For the integrated NPP averaged over the subpolar gyre region (units of mmol N m^{-2} day^{-1}, where N is the nitrogen currency), R12 has the largest NPP at 3.67, compared to CONST at 2.76 and GEOM at 2.91 (respectively a decrease of -24.8% and -20.6% relative to R12). The GEOM calculation results in NPP values closer to the model truth R12 compared to the CONST calculation, which is consistent with our expectations, although the improvements are somewhat modest.

As noted in §2, the biogeochemistry model takes no explicit account of temperature variations on the biogeochemical activities themselves, so the changes observed are a result of the changes in the nutrient distributions. While NPP has contributions from nitrate and ammonium, we focus our attention on nitrate as it is the dominant form of dissolved inorganic nitrogen except in oxygen poor regions in the marine system (e.g. oxygen minimum zones or coastal hypoxia zones). The f-ratio, the ratio between primary production arising from nitrate and total primary production (e.g., Sarmiento and Gruber, 2006, §4), is relatively constant over the set of calculations at around

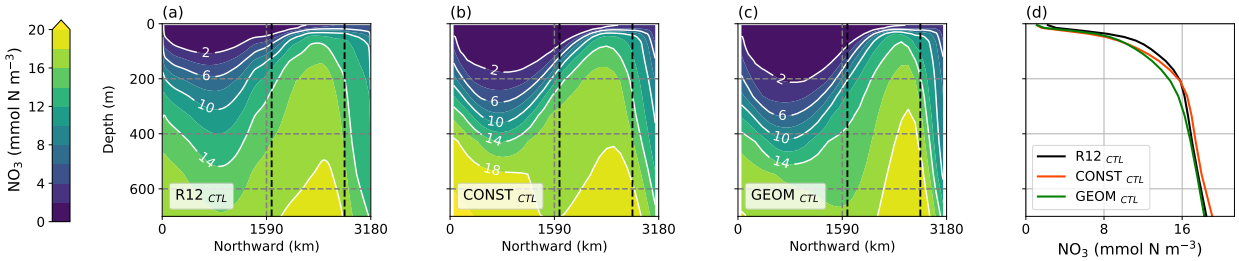

Figure 6: (a, b, c) Vertical distribution of zonally averaged nitrate concentration (NO_3^-, mmol N m^{-3}, where N is the nitrogen currency unit), with lines of constant nitrate marked on. (d) The vertical distribution of nitrate in the predefined subpolar gyre box (see e.g. Fig. 5). The area enclosed by black dashed lines denote the boundaries of the subpolar gyre box mentioned in text.

0.43 (cf. Couespel et al., 2021). We show in Fig. 6 the zonally averaged vertical distribution of nitrate, and we see a suppression and elevation of nitrate concentration in the subtropical and subpolar gyres respectively across all models, consistent with the Ekman downwelling and upwelling from the choice of zonal wind forcing (e.g., §4 of Williams and Follows, 2011). In both the CONST and GEOM calculations, there is a strong decrease in nitrate concentration in the subtropical gyre compared with R12, possibly in line with the damped Western Boundary Current associated with the larger κ_{gm} values in the region. There is also an overall decrease over the whole subpolar gyre in the coarse resolution calculations. However, there is an increase in nitrate concentration in the northern parts of the subpolar gyre for GEOM compared to CONST (examined via the differences; not shown), which collectively leads to a mildly elevated NPP in the same subpolar gyre region in GEOM compared to CONST.

To analyse the transport properties of nitrate, we note that the advective contribution arises as $\nabla \cdot (\boldsymbol{u}N)$, where N denotes the nitrate concentration. Focusing on the subpolar gyre box (area enclosed by the black dashed lines in Fig. 5 and 6), noting that the box boundaries at longitudinal lines coincide with the model domain boundaries, by the divergence theorem and invoking no normal flow boundary conditions, we have

$$\int_{\text{box}} \nabla \cdot (\boldsymbol{u}N)\, \mathrm{d}x\, \mathrm{d}y\, \mathrm{d}z = \left(\int_{\text{south}} + \int_{\text{north}} \right) vN\, \mathrm{d}x\, \mathrm{d}z + \int_{\text{bottom}} wN\, \mathrm{d}x\, \mathrm{d}y. \tag{8}$$

We can further consider the Reynolds decomposition

$$N = \overline{N} + N', \qquad \overline{N'} = 0 \tag{9}$$

where the overbar is still the time average, which leads to

$$\overline{\boldsymbol{u}N} = \overline{\boldsymbol{u}}\,\overline{N} + \overline{\boldsymbol{u}'N'}, \tag{10}$$

respectively the total, the mean and the eddy advective flux of nutrients, and $\boldsymbol{u}'$ is from the explicit velocity fluctuations in the case of explicit eddies, supplemented by parameterised eddy induced velocity $\boldsymbol{u}^*$ when a GM-based parameterisation is active. We compute the vertical distribution of the vertical nitrate supply, i.e.,

$$\int_{y=L_s}^{y=L_n} \int_0^{L_x} \left(\overline{w}\,\overline{N} + \overline{w'N'} \right) \mathrm{d}x\, \mathrm{d}y, \tag{11}$$

where no vertical integration is implied, as well as the vertical cumulative integral of the horizontal nitrate supply at the southern and northern boundaries, i.e.,

$$\int_0^z \int_0^{L_x} \left(\overline{v}\,\overline{N} + \overline{v'N'} \right) \mathrm{d}x\, \mathrm{d}\tilde{z}. \tag{12}$$

Fig. 7 shows the total advective supply of nitrate into the subpolar gyre box in the vertical, at the southern boundary, and northern boundary. The dominant contribution to the total supply is in the mean component, although the eddy component is somewhat significant in the CONST case (not shown here, but see e.g. Couespel et al. 2021, Fig. A5).

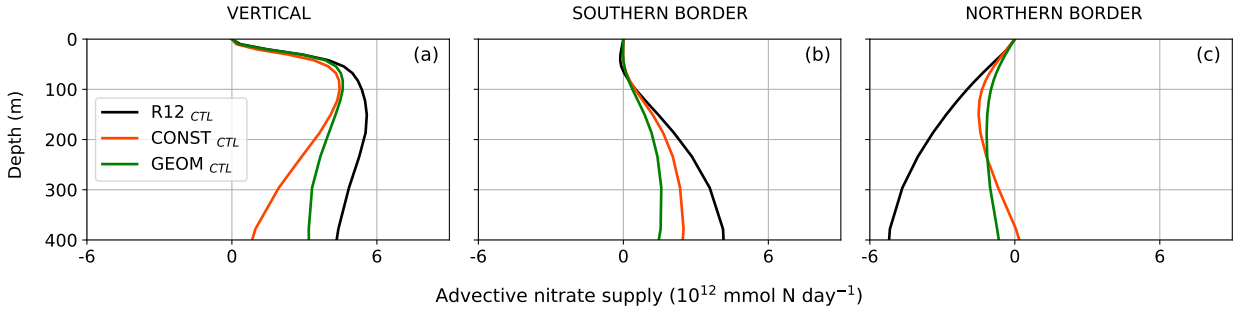

Figure 7: Total advective supply of nitrate (NO_3^-, mmol N day^{-1}, where N is the nitrogen currency unit) into the pre-defined subpolar gyre box. (*a*) Vertical contribution. (*b*) Cumulative southern boundary contribution. (*c*) Cumulative northern boundary contribution. The northern boundary contribution was calculated with an extra minus sign, so positive values indicate a supply into the subpolar gyre box. Lateral and vertical diffusive contributions to nitrate flux are largely similar over the set of calculations and have been omitted.

In all calculations, the vertical nutrient supply rate is dominant over the top 150 m or so (magnitude of positive values, Fig. 7*a*). The vertical mixing contribution dominates over the advective contribution over the top 50 m, but is otherwise similar for the set of calculations (not shown here; cf. Couespel et al. 2021, Fig. 4). However, the meridional nutrient supply becomes important with depth. The model truth R12 has the largest vertical gain (Fig. 7*a*) throughout the depths considered, and the supply from the south and loss from the north (Fig. 7*b*, *c*) are both large, consistent with R12 having the strongest overturning circulation out of the set of calculations considered here (cf. Fig. 3). For the coarse resolution calculations, while the CONST case leads to a meridional gain of nutrients at depths below 200 m via consideration of the residual of the gain from the south and loss from the north, the GEOM case has a larger vertical supply throughout the depths considered, which is more consistent with the R12 calculation, and leads to a larger overall total nutrient concentration, resulting in the larger diagnosed NPP values found in GEOM relative to CONST.

One important point to emphasise here is that while the local eddy contributions are small, it is the eddy feedback onto the mean state and the changes to the mean state that lead to the overall observed response (cf. Couespel et al., 2021). Sample experiments (not shown) show that the NPP *increases* with decreasing κ_{gm}, so one might naïvely argue that we should take κ_{gm} even smaller or even switch it off to improve the eddy component of nutrient supply and increase the NPP. However, this is at the expense of introducing un-physical deep convection into the physical response particularly along the Western Boundary Current, and the mean and eddy components are not isolated components that one can 'tune' separately. The spatially varying nature of κ_{gm} afforded by GEOM allows the GM scheme to adjust according to the physically modelled state, and suppressing its effects in the subpolar gyre where it is potentially detrimental to the biogeochemical response. A calculation with a simpler prescription of κ_{gm} based on Treguier et al. (1997) as implemented into NEMO (which requires a specification of a maximum κ_{gm} and varies in space according to the baroclinic growth rate) was performed here and gives similar conclusions in the control calculation to GEOM (not shown). The resulting κ_{gm} is not unlike that shown in Fig. 2(*c*), but with a much more gradual spatial variation limited by the choice of the maximum κ_{gm}, taken here to be 1000 m^2 s^{-1}. The resulting diagnostics are largely similar and certainly improve upon the CONST case, for reasons detailed already. In that regard, it is the spatially varying nature of κ_{gm} afforded by the more updated schemes that results in a modelled state that is closer to the model truth in the selected diagnostics. However, it is known that schemes based on a prescribed maximum κ_{gm} limits how the models can react to climate change scenarios (e.g., Fox-Kemper et al., 2019). The GEOM scheme and other energetically constrained parameterisations have no such limitations, and we expect such schemes to behave in a favourable way under the climate change scenarios.

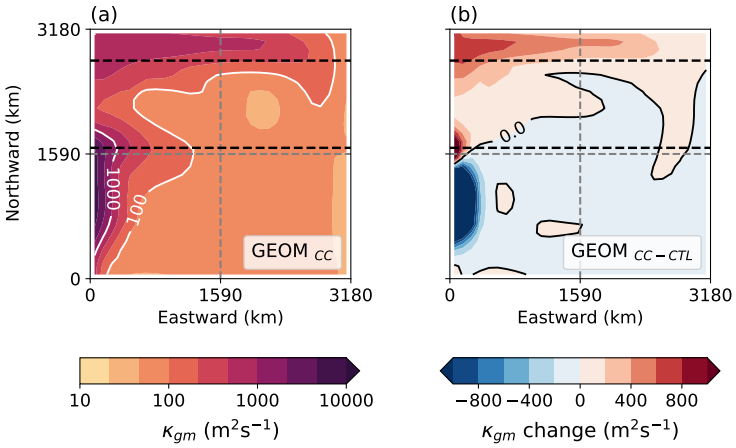

Figure 8: (*a*) The resulting $\kappa_{\rm gm}$ profile associated with GEOM under the climate change experiment, and (*b*) the raw differences of the $\kappa_{\rm gm}$ between the control and the climate change scenario (i.e., Fig. 8*a* minus Fig. 2*c*). Red colours in panel *b* indicate a decrease in $\kappa_{\rm gm}$. The area enclosed by black dashed lines denote the boundaries of the subpolar gyre box mentioned in text.

4. Sensitivities under idealised climate change

4.1. Physical responses

Fig. 8 shows the $\kappa_{\rm gm}$ distribution from GEOM under the climate change scenario, and the raw differences compared to the control scenario. The notable feature here is the increase in $\kappa_{\rm gm}$ towards the northern boundary in Fig. 8(*b*) where the model deep water is formed. Given the discussion in the previous section, we would expect the GEOM calculation in this case to have an over weakened overturning circulation, leading to a decrease in the nutrient supply and the NPP. Details turn out to matter, as will be seen shortly.

Fig. 9(a, b, c) shows the raw differences between the overturning streamfunction under climate change and the control case (cf. Fig. 3a, b, c). While both R12 and GEOM show a significant decrease in the very northern part of the domain, this feature seems to be absent in the CONST case. This lack of decrease in the overturning strength in CONST (and even a mild increase shown at the bottom right half of Fig. 3*b*) might have contributed to the observed sensitivity in the diagnosed northward heat transport: the R12 and GEOM calculations both show only small increases in the heat transport relative to the respective control scenario north of 35° N (+2.0% and +5.7% increase in the area-weighted average respectively), but the CONST calculation shows a rather significant increase in the heat transport in the same region (+23.5% increase in the area-weighted average). The response seen in R12 and GEOM are likely because of the increase in temperature offsetting the decrease in the advective velocity. On the other hand, the magnitude of the response in CONST is quite significant and unlikely to result solely from increases in water temperature, suggesting that the overturning response under climate change scenario in CONST is inconsistent with the actual dynamics in the model truth with explicit eddies.

Fig. 10 shows the changes in the diagnosed maximum mixed layer, and all panels show that the mixed layer depth has generally shoaled across all calculations under the climate change scenario, particularly in the region near the northern boundary. This is consistent with the warming of the atmosphere and the associated decrease in the ocean buoyancy loss. The shoaling is reflected in the shift of the median values, as well as a decrease in the quartile ranges. However, note that the coarse resolution models appear to have a noticeably shallower mixed layer, as seen in the histograms and the median values in Fig. 10(e, f) compared to the R12 calculations with explicit eddies (Fig. 10*d*). From the preceding discussion, we might expect that the decrease of the maximum mixed layer depth is more significant in GEOM given the increase in $\kappa_{\rm gm}$ in the region (cf. Fig. 8*b*), leading to a stronger flattening of isopycnals that acts against the formation of deep mixed layers, impacting the overturning circulation.

We can quantify the magnitude of the overall shoaling by numerically computing the 1-Wasserstein distance $W_1(\mu, \nu)$ (sometimes known as the earth mover's distance, e.g. Villani 2008), which measures the distance between two discrete probability distributions μ and ν (i.e., a measure of the 'difference' between two histograms). Doing

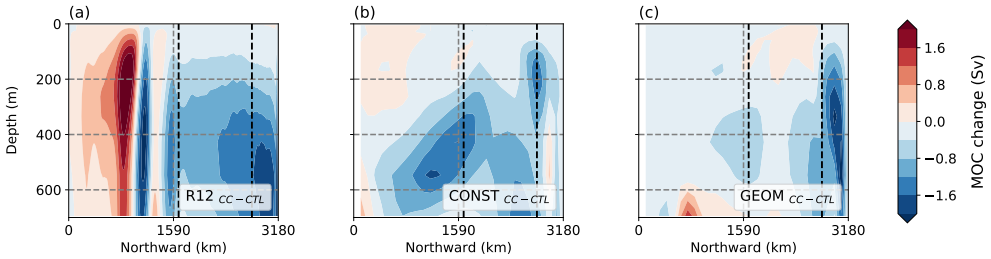

Figure 9: Raw differences of the diagnosed overturning streamfunction Ψ_{MOC} from the climate change scenario with the corresponding control scenario (see Fig. 3, for (*a*) R12, (*b*) CONST, (*c*) GEOM; negative values mostly correspond to a decrease in the overturning strength. The area enclosed by black dashed lines denote the boundaries of the subpolar gyre box mentioned in text. The resulting area-weighted change in the diagnosed northward heat transport north of 35° N given by the southern black dashed line is +2.0%, +23.5% and +5.7% respectively for R12, CONST and CONST.

so leads to $W_1(\mathrm{GEOM_{CTL}}, \mathrm{GEOM_{CC}}) \approx 216$ while $W_1(\mathrm{CONST_{CTL}}, \mathrm{CONST_{CC}}) \approx 170$ in the present mixed layer depth diagnostic, thus supporting the conclusion that the GEOM calculation changes more within the climate change scenario. For completeness, $W_1(\mathrm{R12_{CTL}}, \mathrm{R12_{CC}}) \approx 217$, so in this metric GEOM has a sensitivity that is more in line with R12 than CONST.

4.2. Biogeochemical responses

Fig. 11 shows the horizontal distribution of the raw differences in the vertically integrated NPP between the climate change and control scenarios. There is a decrease in NPP across all models under climate change particularly in the subpolar gyre, although there are isolated spots in the R12 calculation where NPP has marginally increased (south of the Western Boundary Current separation, and at the northern boundary where downwelling occurs). The decrease in NPP in the coarse resolution models are concentrated particularly in the east of the subpolar gyre region, and a small patch towards the western boundary in the GEOM calculation.

The integrated NPP value averaged over the subpolar gyre box declines under climate change for all calculations, with R12 at 3.16 (−13.8%), CONST at 2.13 (−22.9%) and GEOM at 2.22 (−23.6%), where the raw numbers are in units of mmol N m^{-2} day^{-1} (N being the nitrogen currency), and the percentage difference is relative to the respective calculations in the control scenario. The R12 model simulates the largest NPP overall, with the smallest decline under the climate change scenario. The coarse resolution models significantly under predict the raw value of the NPP, and also predict a more dramatic decline, in line with the previous results of Couespel et al. (2021). While it is true that the GEOM calculation still predicts a higher NPP than the CONST calculation in both the control and climate change scenario, the GEOM calculation displays more sensitivity to the change in forcing under the climate change scenario, with a marginally larger NPP decline compared to CONST. Although the relative decrease in NPP in CONST is smaller in magnitude than GEOM, we should also bear in mind that there is evidence indicating that CONST possesses a sensitivity in the physical response that is inconsistent with the eddy resolving calculation R12 (e.g. Fig. 9), i.e., the CONST calculation might be "better" in the integrated NPP diagnostic, but not necessarily for the right reasons.

The observed decline in NPP can again be attributed to the changes in the nutrient supply. We focus our attention again on nitrate; there is a decrease in the f-ratio to around 0.40 (from around 0.43 in the control scenario) uniformly across the set of calculations. Fig. 12 shows the differences in vertical distribution of zonally averaged nitrate between the climate change and control scenario (see also Fig. 6). There is a decline of nitrate in the upper portions of the subpolar gyre across all models, with a mild increase at depths, indicating a decline in upwelling consistent with the strengthened stratification, as indicated for example by the buoyancy frequency $N^2 \sim -\partial\rho/\partial z$ (not shown; cf. Fig. A10 of Couespel et al. 2021). Fig. 12(*d*) shows the vertical distribution of the nitrate concentration averaged over the subpolar gyre box, and it is noteworthy that the GEOM calculation has a vertical distribution change that is closer to the model truth R12 than the CONST case.

The differences in the total advective fluxes into the subpolar gyre box (relative to the diagnosed supplies in Fig. 7) are shown in Fig. 13; the dominant contribution to the total change was again found to be in the mean, although the

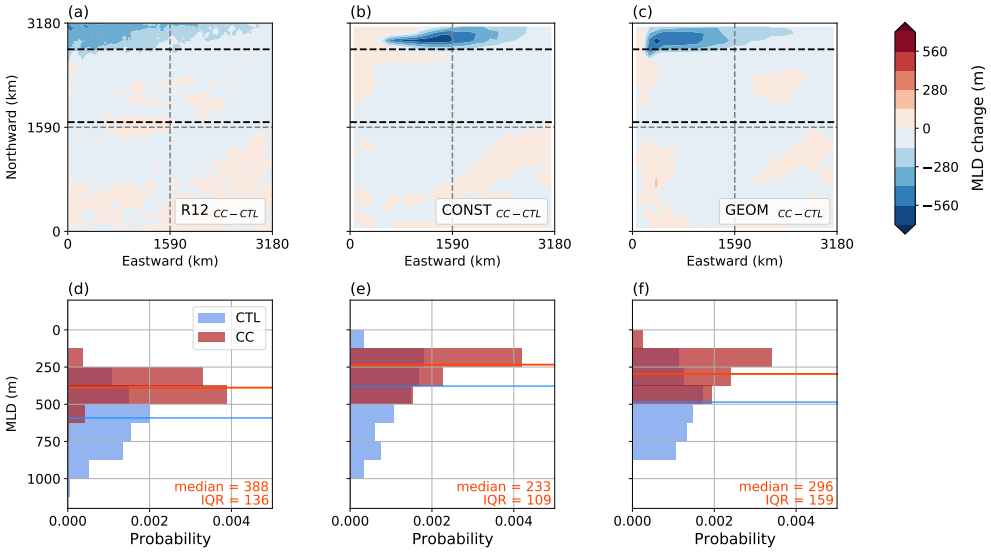

Figure 10: (Top row) Raw difference between climate change and control scenario maximum mixed layer depth (m, diagnosed as the first depth below which $|\sigma_\theta(z) - \sigma_\theta(z = -10\,\mathrm{m})| > 0.01$, where σ_θ is the potential density referenced to sea level), for (*a*) R12, (*b*) CONST and (*c*) GEOM; red colours denote a decrease in mixed layer depth (i.e., shoaling of the mixed layer). The area enclosed by black dashed lines denote the boundaries of the subpolar gyre box mentioned in text. (Bottom row) Histogram of the mixed layer depth distributions and median (marked on as a line) over the subpolar gyre region of both the climate change scenario (in red) and histogram of control scenario (in blue, cf. Fig. 4*d*, *e*, *f*) for (*d*) R12, (*e*) CONST and (*f*) GEOM; the axes of the histograms have been swapped to enable ease of visual comparison.

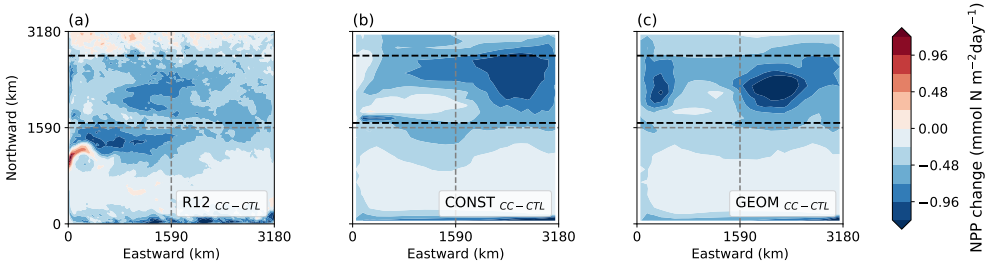

Figure 11: Raw differences of the vertically integrated Net Primary Production (NPP, mmol N m^{-2} day^{-1}, where N is the nitrogen currency) between the climate change scenario and the control scenario (Fig. 5*a*, *b*, *c*) for (*a*) R12, (*b*) CONST and (*c*) GEOM. The area enclosed by black dashed lines denote the boundaries of the subpolar gyre box mentioned in text.

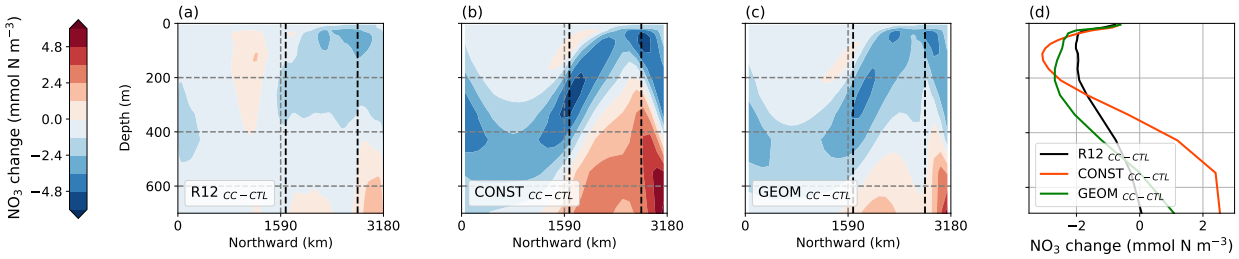

Figure 12: Raw differences between the vertical distribution of zonally averaged nitrate concentration (NO_3^-, mmol N m^{-3}, where N is the nitrogen currency unit) between the climate change scenario and the control scenario (Fig. 6*a*, *b*, *c*) for (*a*) R12, (*b*) CONST and (*c*) GEOM; red values denote a decrease in nitrate concentration. The area enclosed by black dashed lines denote the subpolar gyre box mentioned in text. (*d*) Raw differences in the vertical distribution of nitrate in the predefined subpolar gyre box between the climate change scenario and the control scenario (Fig. 6*d*).

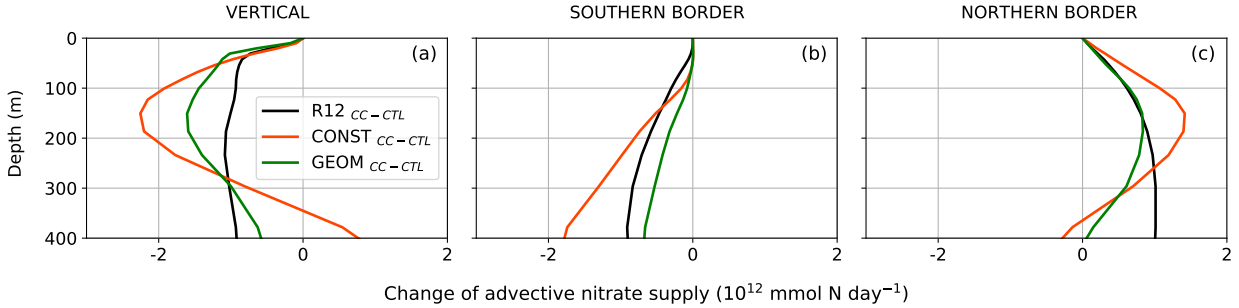

Figure 13: Differences of the total advective supply of nitrate (NO_3^-, mmol N day^{-1}, where N is the nitrogen currency unit) into the pre-defined subpolar gyre box between the climate change and control scenario (cf. Fig. 13). (*a*) Vertical contribution. (*b*) Cumulative southern boundary contribution. (*c*) Cumulative northern boundary contribution. Negative values here largely mean a *decrease* in the supply into the subpolar gyre, while positive values mostly mean a *decrease* in the loss out of the subpolar gyre. Lateral and vertical diffusive contributions to nitrate flux are largely similar over the set of calculations and have been omitted.

eddy component is somewhat sizeable for the CONST case. Note that negative values in Fig. 13 largely mean a *decrease in the supply* into the subpolar gyre, while positive values mostly mean a *decrease in the loss* out of the subpolar gyre; the changes in the diffusive contributions are largely similar across the set of calculations and have been omitted. The R12 case has a decreased vertical nutrient supply (Fig. 13*a*), southern boundary gain (Fig. 13*b*) and northern boundary loss (Fig. 13*c*) under idealised climate change, broadly consistent with a decrease in the overturning strength (cf. Fig. 9). For the coarse resolution calculations, we note that while CONST suffers a large decrease in the vertical supply over the top 300 m (Fig. 13*a*), it seems to be compensated by an equally large decrease in the northern boundary loss over the same depths (Fig. 13*c*). This is particularly interesting, given neither of these sensitivities are nearly as dramatic in the R12 calculation, and suggests that this is a case where two "wrongs" happen to cancel out, resulting in a reasonable integrated response in the NPP. On the other hand, the GEOM calculation over most panels capture the shape of the R12 responses somewhat (and arguably substantially improve on the sensitivities displayed by the CONST calculation), except at the northern boundary below 200 m, and there is a notable decrease in the vertical supply in the upper 50 m of the ocean. While the GEOM calculation seems to respond in a way that is more consistent with the model truth, it seems to (*i*) do things 'wrong' perhaps where it matters the most in the vertical nutrient supply (upper part of the ocean where light availability and NPP are the largest), and (*ii*) not have the benefit of two 'wrongs' cancelling out as in the CONST case.

5. Conclusions and discussions

Numerical ocean models at non-eddy resolving to partially eddy permitting resolutions, requiring sub-grid physics parameterisation of the mesoscale processes, are going to remain the norm for the foreseeable future. Assessment of related parameterisations to highlight the possible benefits and deficiencies are required to constrain our uncertainties in the relevant conclusions and projections to be drawn from such models. To that end, this work presents an investigation of the joint physical and biogeochemical sensitivity to the choice of mesoscale eddy parameterisation in light of the recent developments in eddy parameterisation and its improvements into the modelled physical processes. The focus here is the more conventional diffusive closures utilised in coarse resolution non-eddy permitting ocean models, principally on the eddy induced advection represented by the GM scheme (e.g., Gent and McWilliams, 1990; Gent et al., 1995) and the GM version of the GEOMETRIC scheme (Marshall et al., 2012; Mak et al., 2018, 2022b). The latter takes a κ_{gm} that scales linearly with eddy energy (Eq. 3) and constrained by a parameterised eddy energy budget (Eq. 4). The present work highlights a need to evaluate the performance and tuning of eddy parameterisations on both the physical and biogeochemical response, and documents the performance of diffusive closures in coarse resolution models and the eddy resolving model truth as a precursor to an assessment into the eddy-permitting models as well as backscatter-type parameterisations.

To comprehensively assess the impacts afforded by the choice of mesoscale eddy parameterisation, this investigation employs a simplified and well-understood physical model (a double gyre configuration with a prescribed seasonal pattern leading to deep water formation near the northern boundary). Further, a simplified biogeochemistry model was chosen to focus on the chain of causality relating sensitivities afforded by the eddy parameterisation, its impact on the modelled state, its consequences for nutrient supply (e.g., Williams et al., 2017, 2011; Whitt and Jansen, 2020; Gupta et al., 2022), and in turn Net Primary Production (NPP). The choice of an idealised model with limited spatial extent allows for an eddy resolving model truth for coarse resolution models to compare against. The general model behaviours are entirely consistent with those reported in Couespel et al. (2021), where NPP decreases under the climate change scenario. This was attributed to the strengthening of upper ocean stratification, leading to a weakened overturning circulation, and thus weakening of nutrient supply into the subpolar gyre region where the NPP is strongest. The coarse resolution models display a more significant decrease in the NPP, attributed to a weaker overturning circulation in the coarse resolution models. The previous work was performed with the standard prescription of the GM scheme with a constant GM coefficient, and this work extends it in the first instance by considering a more updated GM-based eddy parameterisation, as well as critically assessing the model sensitivities as a result of the parameterisations, and in anticipation of assessing model performance in eddy permitting models.

A summary of the key diagnostics in this work and a comparison of the more updated GM-based eddy parameterisation with the constant case is given in Table 2. We have not found evidence for significant internal variability beyond the annual forcing period, which may be because of the choice of model and forcing set up, which only has a repeating seasonal cycle. While the reported diagnostics and conclusions should be considered statistically significant, we emphasise again that the main focus here is on the qualitative relative differences (e.g. differences in modelled state and/or sensitivities) and less on the quantitative absolute values (e.g. magnitude of differences in modelled state and/or sensitivities). The latter will be somewhat context dependent, so should be performed with a more realistic model for constraining climate projections.

The first main finding here is that the GM-version of the GEOMETRIC scheme (Marshall et al., 2012), which was found previously to lead to improved sensitivities in the modelled ocean mean state particularly when the domain includes a representation of the Southern Ocean (Mak et al., 2018, 2022b), leads to an improvement over the case where the GM coefficient κ_{gm} is set to be uniform over space, largely because the resulting κ_{gm} varies in space and is somewhat state-aware. The benefits afforded by a spatially varying κ_{gm} with reasonable properties are not entirely surprising and are somewhat known in the physical oceanography modelling community, though perhaps not so widely reported. In this particular model, the overall model response seems to be particularly sensitive to the value of κ_{gm} in the region with deep water formation, which is consistent with theoretical considerations through the impact on the overturning circulation (e.g., Williams and Follows, 2011). Extra calculations reported in Appendix A with prescribed spatially varying κ_{gm} further support the reported model responses. The observed model effect is rationalised here as the eddy induced advection acting against deep water formation and associated convective events, and a smaller κ_{gm} is conducive to deeper mixed layers and a stronger overturning circulation. The resulting state from using GEOMETRIC with $\kappa_{\mathrm{gm}} \sim E$ (where E is the total eddy energy) under the control scenario has a marginally stronger overturning

Diagnostic	R12 values	CONST values	GEOM values	improve over CONST
overturning circulation (Sv)				
(Fig. 3a, b, c and 9a, b, c)				
L^2 mismatch rel. R12 (CTL)	—	2.29	1.99	✓
L^2 mismatch rel. R12 (CC)	—	1.87	1.63	✓
northward heat transport (10^{15} W)				
(Fig. 3d, e, f and 9d, e, f)				
area average (CTL)	0.146	0.078	0.094	✓
area average (CC)	0.148 (+2.0%)	0.097 (+23.5%)	0.099 (+5.7%)	✓ (✓)
sensitivity (L^2)	0.004	0.020	0.006	✓
northern mixed layer depth (m)				
(Fig. 4 and 10)				
median (CTL)	592	378	486	✓
median (CC)	388 (−34.8%)	234 (−38.2%)	296 (−39.0%)	✓ (×)
quartile range (CTL)	285	376	399	×
quartile range (CC)	137 (−51.9%)	110 (−70.9%)	160 (−60.0%)	× (✓)
sensitivity (1-Wasserstein)	217	170	216	✓
NPP (mmol N m^{-2} day^{-1})				
(Fig. 5 and 11)				
area average (CTL)	3.67	2.76	2.91	✓
area average (CC)	3.16 (−13.8%)	2.13 (−22.9%)	2.22 (−23.6%)	✓ (×)
NO_3^- concentration (mmol N m^{-3})				
(Fig. 6d and 12d)				
area average (CTL)	15.61	15.57	15.01	×
area average (CC)	14.54 (−6.9%)	15.48 (−0.6%)	13.70 (−8.7%)	× (✓)
sensitivity (L^2)	1.31	2.14	1.84	✓

Table 2: Summary of diagnostics and their sensitivities for the set of calculations, where the bracketed numbers denote the percentage differences of the diagnostic between the climate change (CC) and control (CTL) scenario, and L^2 denotes the area-weighted average root-mean-square difference (and has the same units as the diagnostics themselves).

circulation (Fig. 3) and more consistent statistics in the mixed layer depths (Fig. 4). This leads to a higher nutrient supply rate and NPP (Table 2), with modelled nutrient transport properties (Fig. 7) that are more consistent with the model truth over the CONST case. It was verified in the extra calculations with the Treguier et al. (1997) prescription of κ_{gm} (choosing maximum κ_{gm} value to be 1000 m^2 s^{-1}) leads to qualitatively similar results as GEOM in the control calculation (not shown). We would expect similar eddy parameterisation schemes employing mixing length arguments with $\kappa_{\text{gm}} \sim \sqrt{K}$ (where K is the eddy kinetic energy), such as parts of MEKE (Jansen et al., 2019), to lead to qualitative similar results as GEOM here, although this has not been verified.

The second finding, one that is more subtle, is that a better physical response does not guarantee a better biogeochemical response, and a better biogeochemical response could arise from physically inconsistent physical responses, so there is a need to evaluate eddy parameterisations based on responses in both. The GM-version of the GEOMETRIC scheme does 'worse' in the integrated NPP metric to idealised climate change compared to the standard implementation, even though the model using the GEOMETRIC scheme actually seems to mostly improve on the bulk sensitivities as displayed by the model truth (e.g. nitrate concentration in Fig. 12, nutrient supply profiles in Fig. 13), and certainly more convincing and consistent than the CONST case (which was found to have a significant increase in the heat transport and different advective nutrient supply profiles). The observation here seems to stem from (*i*) the standard prescription of GM, while producing inconsistent sensitivities, happen to lead to cancellations (e.g. strong

decrease in supply of nutrient at southern boundary, Fig. 13*b*, offset by an even stronger decrease in loss of nutrient at northern boundary, Fig. 13*c*), and (*ii*) the GEOMETRIC scheme happens to lead to a change in regions that are particularly important to the model response (increase in the $\kappa_{\rm gm}$ towards the northern boundary, Fig. 8, and decrease in the vertical nutrient supply near the top of the ocean, Fig. 13*a*). Extra calculations with the Treguier et al. (1997) prescription of $\kappa_{\rm gm}$ with no re-tuning leads to diagnostics that are qualitatively close to the GEOM calculations, but at a lesser magnitude, so that the integrated results are somewhat better than GEOM (not shown). The better performance in NPP diagnostics however is likely because the resulting $\kappa_{\rm gm}$ is still artificially capped at the same value, so that the influence of $\kappa_{\rm gm}$ over the northern boundary region is muted compared with GEOM. We would expect similar eddy parameterisation schemes employing mixing length arguments with $\kappa_{\rm gm} \sim \sqrt{K}$ would do slightly better in the integrated NPP diagnostics than GEOM because of the more muted increase in $\kappa_{\rm gm}$ over the northern boundary region, although this has not been verified here.

One key point we make here is that care needs to be taken in the choice of metric to judge on the performance, and a combination of metrics might be required to highlight the intricacies of the model behaviour that are potentially masked behind a single metric, particularly when an average or integrated quantity is used. A case in hand here is that while the standard prescription of the GM scheme seems to lead to a 'better' response in integrated NPP, it is masking the fact that the contributing sensitivities are largely inconsistent with the model truth, i.e., two 'wrongs' can result in something that appears to look 'right'. Ultimately the requirement should be that the biogeochemistry response is 'better' because the underlying ocean physics is 'better', and this work highlights a cautionary example where ocean models investigating biogeochemical responses should evaluate the modelled physical responses where possible.

The present use of an idealised model, in addition to providing a clean investigation into the strengths and deficiencies in the parameterisation schemes, also highlights lessons that we can learn from when extending our investigation to more complex but realistic models. If a GM-based parameterisation scheme is to be used in more realistic models, some form of tapering of $\kappa_{\rm gm}$ might be required as the regions of deep water formation are approached (cf. Hallberg, 2013), since this can have knock-on effects for the overturning circulation and affect biogeochemical responses in a non-local fashion. More complex biogeochemistry models are required to assess and highlight the impact of eddy parameterisations on the modelled biogeochemistry, for example carbon and oxygen budgets (e.g., Friedlingstein et al., 2014; Berthet et al., 2019; Séférian et al., 2019; Kwiatkowski et al., 2020). Our focus here is more process oriented, and to set out a framework for evaluating the qualitative model responses and sensitivities to parameterisation, but the use of more complex and realistic models are required for quantifying uncertainties in projections, and will be a future focus.

Another choice made here is to focus on the eddy induced advection as represented by the GM scheme, sidelining the isoneutral diffusion as represented by the Redi scheme (e.g. Redi, 1982; Griffies, 1998). It is somewhat considered in the modelling community that the GM coefficient impacts the ventilation pathways via changes to the stratification profile, and in turn the rate of ventilation, while the isoneutral diffusion affects mostly the rate of ventilation (e.g., England and Rahmstorf, 1999; Matear, 2001; Gnanadesikan et al., 2015; Jones and Abernathey, 2019) without significantly affecting the modelled state (but see Chouksey et al. 2022). Theoretical developments as well as numerical assessment of the GM-based schemes are somewhat more active and mature (e.g., Eden and Greatbatch, 2008; Hofman and Morales Maqueda, 2011; Mak et al., 2018; Jansen et al., 2019; Bachman, 2019) compared to that of isoneutral diffusion (e.g., Smith and Marshall, 2009; Ferrari and Nikurashin, 2010; Abernathey et al., 2013; Groeskamp et al., 2021). With that in mind prior to our investigation, we have mostly focused on the GM-based schemes, but we considered simulations varying the spatially constant isoneutral diffusion coefficient $\kappa_{\rm iso}$. Our sample simulations varying the spatially constant $\kappa_{\rm iso}$ by itself seems to have very minor to negligible impacts for this model, but there are feedback loops present if $\kappa_{\rm gm}$ is state-aware (see Appendix A). A systematic and comprehensive assessment of the isoneutral diffusion parameterisation schemes is a major undertaking, and we opted to postpone the related investigation.

While we would like to make use of mesoscale resolving models generally, these are still computationally prohibitive and likely to remain so for the foreseeable future. As a compromise, there is an increasing focus on eddy permitting models, to broadly refer to ocean models around $1/2^\circ$ to $1/9^\circ$ horizontal resolution, where mesoscale eddies have an explicit but incomplete representation (e.g. the explicit eddy field is substantially less energetic, from measures such as the explicit eddy kinetic energy). As noted at the beginning of this work, existing geostrophic mesoscale eddy parameterisations largely split into diffusive closures, which was the subject of this present work,

and backscatter approaches (e.g., Bachman, 2019; Jansen et al., 2019). The former is more targeted towards coarse resolution model without an explicit representation of eddies (e.g. models with around 1° horizontal resolution, such as the NEMO ORCA1 model). The latter in principle should work across models at different resolutions, but the working consensus at the time of writing seems to be that backscatter approaches work better in eddy permitting models, energising the eddies that are explicitly represented by the model itself. Given the increase in available computational power for performing global ocean models and Earth System Models at eddy permitting resolutions (normally around 1/4° horizontal resolution), and the benefits that result once ocean models start to become eddy permitting (e.g., Hewitt et al., 2017, 2020), an assessment into backscatter parameterisations analogous to the one carried out here is a priority, and is currently the subject of investigation.

Acknowledgements

This research was supported by Southern Marine Science and Engineering Guangdong Laboratory (Guangzhou) (SMSEGL20SC01) and the RGC General Research Fund 16304021. DC is funded by the Research Council of Norway under grant 275268 (COLUMBIA). ML acknowledges financial support from the Chanel Research Chair of ENS-PSL. The numerical model modifications, analyses code and sample model data including those mentioned in text but not shown may be found on Zenodo at `http://dx.doi.org/10.5281/zenodo.7612270`.

Appendix A. Model dependence on other parameters

Here we provide some further evidence for our assertion that the model mostly depends on κ_{gm}, particularly its values around the northern boundary where deep water formation occurs, and a brief description of model dependence on other key uncertain parameters within the system, namely the GEOMETRIC parameters α and λ (see Eq. 3 and 4), and the isoneutral diffusion parameter κ_{iso}.

The dynamical argument here is that the presence of κ_{gm} leads to the flattening of isopycnals at the base of the mixed layer, which inhibits the deepening of mixed layers. Such an effect leads to a shallow bias of the mixed layer depths, a weakening of the overturning circulation, a reduction in nutrient supply and a reduction in NPP. The argument is in line with the previous results in the Appendix of Couespel et al. (2021), as well as our CONST experiments, where it is generally observed that the smaller the κ_{gm}, the higher the NPP (for precisely the aforementioned dynamical reasons, with signatures in the mixed layer depths and other physical metrics; not shown). The highest NPP occurs for the case when the GM scheme is completely switched off, but of course at the expense of introducing un-physical deep convection around the domain, as mentioned in the text.

It follows that varying the GEOM parameters α and λ affect the resulting model results in a way that is consistent with varying κ_{gm} (varying the energy diffusion coefficient η_E leads to fairly weak responses in $\kappa_{\mathrm{gm}} \sim E$ via modifying the sharpness of the modelled total eddy energy signature E). Increasing α and decreasing λ (or increasing the dissipation time-scale λ^{-1}) both lead to increased κ_{gm} (consistent with Mak et al. 2017; see Marshall et al. 2017 for physical rationalisation), leading to decreases in NPP again for the aforementioned reasons. While the resulting modelled state under the control scenario differ depending on the choice of GEOM parameters, the resulting sensitivities under climate change for fixed choices of α and λ are largely similar in magnitude, with a similar decrease in NPP, again because of the resulting increase in the κ_{gm} value over the northern boundary region. Although there are no strong constraints on the choice of α and λ (but see attempts in Poulsen et al. 2019 and Mak et al. 2022a), it is at least reassuring that the conclusions regarding the sensitivity under climate change scenarios are robust.

The sensitivity of the modelled state to the κ_{gm} value at the northern boundary was further supported by results from experiments where κ_{gm} was artificially enhanced/suppressed under the climate change scenario, via manually modifying the CONST or GEOM κ_{gm} profiles in various regions. All results are consistent with the fact that increased κ_{gm} at the northern boundary lead to decreased NPP for the physical chain of causality detailed above. Further, the results support the notion that GEOM produces 'better' results in the control scenario because of the spatially varying κ_{gm}, but is perhaps over responding under the climate change scenario, as suggested in text.

Regarding sensitivity to the isoneutral diffusion, for lack of strong evidence to suggest which prescription functions the best, we opted to study the simple case of varying the constant diffusion coefficient κ_{iso}. Table A.3 documents the diagnosed NPP in the various scenarios, for both the CONST (which are results implicitly reported in the Appendix of

		NPP (CTL)	NPP (CC)	ΔNPP (self)
CONST	$\kappa_{\rm iso}$ = 500	2.73	2.16	−20.7%
	$\kappa_{\rm iso}$ = 1000	2.76	2.13	−22.9%
	$\kappa_{\rm iso}$ = 2000	2.87	2.22	−22.9%
GEOM	$\kappa_{\rm iso}$ = 500	2.75	2.06	−25.1%
	$\kappa_{\rm iso}$ = 1000	2.91	2.22	−23.6%
	$\kappa_{\rm iso}$ = 2000	3.11	2.48	−20.4%

Table A.3: Integrated Net Primary Production rate (NPP, mmol N m^{-2} day^{-1}, where N is the nitrogen currency) integrated over the subpolar gyre box under the climate change scenario, for various calculations with varying $\kappa_{\rm iso}$.

Couespel et al. 2021) and GEOM calculations. The general conclusions here are that increasing $\kappa_{\rm iso}$ leads to increased NPP, which is consistent with the increased transport of nutrients (at least in the lateral direction in the present gyre setting), certainly in the control scenario, and is suggestive in the climate change scenario. The observed sensitivity to $\kappa_{\rm iso}$ are stronger in the GEOM case, which arises from the nonlinear state dependence of $\kappa_{\rm gm}$. In the CONST case $\kappa_{\rm gm}$ and $\kappa_{\rm iso}$ are independently prescribed, and the resulting modelled states at different $\kappa_{\rm iso}$ are not so different between the experiments at least from a qualitative point of view (and consistent with the conclusions of Couespel et al. 2021). On the other hand, in the GEOM case, increases in $\kappa_{\rm iso}$ leads to minor differences in the modelled state, which leads to changes in the calculated $\kappa_{\rm gm}$ (in this case a *decreasing* $\kappa_{\rm gm}$ over the northern boundary region, but with only very minor changes elsewhere in terms of the spatial pattern), which modifies onto the modelled state, leading to a modified $\kappa_{\rm gm}$. The claim here is that the changes in the NPP we are seeing in GEOM from changing $\kappa_{\rm iso}$ arise from a positive feedback loop through its impact on $\kappa_{\rm gm}$ and resulting changes in the modelled stratification. The present nonlinear feedback loop between $\kappa_{\rm iso}$, the modelled state and $\kappa_{\rm gm}$ arising from GEOM should be studied further but is beyond the scope of the present work.

References

Abernathey, R., Ferreira, D., Klocker, A., 2013. Diagnostics of isopycnal mixing in a circumpolar channel. Ocean Modell. 72, 1–16.

Adcroft, A., Anderson, W., Bushuk, C. B. M., Dufour, C. O., Dunne, J. P., Griffies, S. M., Hallberg, R. W., Harrison, M. J., Held, I., Jansen, M. F., John, J., Krasting, J. P., Langenhorst, A., Legg, S., Liang, Z., McHugh, C., Radhakrishnan, A., Reichl, B. G., Rosati, T., Samuels, B. L., Shao, A., Stouffer, R., Winton, M., Wittenberg, A. T., Xiang, B., Zadeh, N., Zhang, R., 2019. The GFDL global ocean and sea ice model OM4.0: Model description and simulation features. J. Adv. Model. Earth. Syst. 11, 3167–3211.

Bachman, S. D., 2019. The GM+E closure: A framework for coupling backscatter with the Gent and McWilliams parameterization. Ocean Modell. 136, 85–106.

Bachman, S. D., Marshall, D. P., Maddison, J. R., Mak, J., 2017. Evaluation of a scalar transport coefficient based on geometric constraints. Ocean Modell. 109, 44–54.

Bates, M., Tulloch, R., Marshall, J., Ferrari, R., 2014. Rationalizing the spatial distribution of mesoscale eddy diffusivity in terms of mixing length theory. J. Phys. Oceanogr. 44, 1523–1540.

Bellomo, K., Angeloni, M., Corti, S., von Hardenberg, J., 2021. Future climate change shaped by inter-model differences in Atlantic meridional overturning circulation response. Nat. Commun. 12 (1), 1–10.

Berloff, P., 2005. On rectification of randomly forced flows. J. Mar. Res. 63, 497–527.

Berthet, S., Séférian, R., Bricaud, C., Chevallier, M., Voldoire, A., Ethé, C., 2019. Evaluation of an online grid-coarsening algorithm in a global eddy-admitting ocean biogeochemical model. J. Adv. Model. Earth Syst. 11, 1–25.

Bindoff, N. L., McDougall, T. J., 1994. Diagnosing climate change and ocean ventilation using hydrographic data. J. Phys. Oceanogr. 24 (6), 1137–1152.

Bonan, G. B., Doney, S. C., 2018. Climate, ecosystems, and planetary futures: The challenge to predict life in Earth system models. Science 359, eaam8328.

Bopp, L., Resplandy, L., Orr, J. C., Doney, S. C., Dunne, J. P., Gehlen, M., annd C. Heinze, P. H., Ilyina, T., Séférian, R., Tjiputra, J., Vichi, M., 2013. Multiple stressors of ocean ecosystems in the 21st century: projections with CMIP5 models. Biogeosciences 10, 6225–6245.

Bopp, L., Resplandy, L., Untersee, A., Le Mezo, P., Kageyama, M., 2017. Ocean (de)oxygenation from the Last Glacial Maximum to the twenty-first century: insights from Earth System models. Phil. Trans. R. Soc. A 375, 20160323.

Cessi, P., 2008. An energy-constrained parametrization of eddy buoyancy flux. J. Phys. Oceanogr. 38, 1807–1819.

Chelton, D. B., Schlax, M. G., Samelson, R. M., 2011. Global observations of nonlinear mesoscale eddies. Prog. Oceanog. 91, 167–216.

Chouksey, A., Grisel, A., Chouksey, M., Eden, C., 2022. Changes in global ocean circulation due to isopycnal diffusion. J. Phys. Oceanogr. 52, 2219–2235.

Couespel, D., Lévy, M., Bopp, L., 2021. Oceanic primary production decline halved in eddy-resolving simulations of global warming. Biogeosciences 18, 4321–4349.

Danabasoglu, G., McWilliams, J. C., Gent, P. R., 1994. The role of mesoscale tracer transports in the global ocean circulation. Science 264, 1123–1126.
de Boer, A. M., Sigman, D. M., Toggweiler, J. R., Russell, J. L., 2007. Effect of global ocean temperature change on deep ocean ventilation. Paleoceanography 22, 1–15.
Doney, S. C., Ruckelshaus, M., Duffy, J. E., J. P. Barry, F. C., English, C. A., Galindo, H. M., Grebmeier, J. M., Hollowed, A. B., Knowlton, N., Polovina, J., Rabalais, N. N., Sydeman, W. J., Talley, L. D., 2012. Climate change impacts on marine ecosystems. Ann. Rev. Mar. Sci. 4, 11–37.
Eden, C., Greatbatch, R. J., 2008. Towards a mesoscale eddy closure. Ocean Modell. 20, 223–239.
England, M. H., Rahmstorf, S., 1999. Sensitivity of ventilation rates and radiocarbon uptake to subgrid-scale mixing in ocean models. J. Phys. Oceanogr. 29, 2802–2828.
Farneti, R., Downes, S. M., Griffies, S. M., Marsland, S. J., Behrens, E., Bentsen, M., Bi, D., Biastoch, A., Böning, C. W., Bozec, A., Canuto, V. M., Chassignet, E., Danabasoglu, G., Danilov, S., Diansky, N., Drange, H., Fogli, P. G., Gusev, A., Hallberg, R. W., Howard, A., Ilicak, M., Jung, T., Kelley, M., Large, W. G., Leboissetier, A., Long, M., Lu, J., Masinam, S., Mishra, A., Navarra, A., Nurser, A. J. G., Patara, L., Samuels, B. L., Sidorenko, D., Tsujino, H., Uotila, P., Wang, Q., Yeager, S. G., 2015. An assessment of Antarctic Circumpolar Current and Southern Ocean meridional overturning circulation during 1958-2007 in a suite of interannual CORE-II simulations. Ocean Modell. 94, 84–120.
Ferrari, R., Nikurashin, M., 2010. Suppression of eddy diffusivity across jets in the southern ocean. J. Phys. Oceanogr. 40, 1501–1519.
Ferreira, D., Marshall, J., Heimbach, P., 2005. Estimating eddy stresses by fitting dynamics to observations using a residual-mean ocean circulation model and its adjoint. J. Phys. Oceanogr. 35, 1891–1910.
Fox-Kemper, B., Adcroft, A. J., Böning, C. W., Chassignet, E. P., Curchitser, E. N., Danabasoglu, G., Eden, C., England, M. H., Gerdes, R., Greatbatch, R. J., Griffies, S. M., Hallberg, R. W., Hanert, E., Heimbach, P., Hewitt, H. T., Hill, C. N., Komuro, Y., Legg, S., Le Sommer, J., Masina, S., Marsland, S. J., Penny, S. G., Qiao, F., Ringler, T. D., Treguier, A. M., Tsujino, H., Uotila, P., Yeager, S. G., 2019. Challenges and prospects in ocean circulation models. Front. Mar. Sci. 6, 65.
Friedlingstein, P., Meinshausen, M., Arora, V. K., Jones, C. D., Anav, A., Liddicoat, S. K., Knutti, R., 2014. Uncertainties in CMIP5 climate projections due to carbon cycle feedbacks. J. Climate 27, 511–526.
Gaspar, P., Grégoris, Y., Lefevre, J., 1990. A simple eddy kinetic energy model for simulations of the oceanic vertical mixing: Tests at station papa and long-term upper ocean study site. J. Geophys. Res. 95, 16179–16193.
Gent, P. R., McWilliams, J. C., 1990. Isopycnal mixing in ocean circulation models. J. Phys. Oceanogr. 20, 150–155.
Gent, P. R., Willebrand, J., McDougall, T. J., McWilliams, J. C., 1995. Parameterizing eddy-induced tracer transports in ocean circulation models. J. Phys. Oceanogr. 25, 463–474.
Gnanadesikan, A., Pradal, M., Abernathey, R., 2015. Isopycnal mixing by mesoscale eddies significantly impacts oceanic anthropogenic carbon uptake. Geophys. Res. Lett. 42 (11), 4249–4255.
Griffies, S. M., 1998. The Gent–McWilliams skew flux. J. Phys. Oceanogr. 28, 831–841.
Groeskamp, S., LaCasce, J. H., McDougall, T. J., Rogé, M., 2021. Full-depth global estimates of ocean mesoscale eddy mixing from observations and theory. Geophys. Res. Lett. 47, e2020GL089425.
Grooms, I., 2015. A computational study of turbulent kinetic energy transport in barotropic turbulence on the f-plane. Phys. Fluids 27, 101701.
Gula, J., Molemaker, M. J., McWilliams, J. C., 2015. Topographic vorticity generation, submesoscale instability and vortex street formation in the Gulf Stream. Geophys. Res. Lett. 42, 4654–4062.
Gupta, M., Williams, R. G., Lauderdale, J. M., Jahn, O., Hill, C., Dutkiewicz, S., Follows, M. J., 2022. A nutrient relay sustains subtropical ocean productivity. Proc. Natl Acad. Sci. USA 119 (41), e2206504119.
Hallberg, R., 2013. Using a resolution function to regulate parameterizations of oceanic mesoscale eddy effects. Ocean Modell. 72, 92–103.
Helm, K. P., Bindoff, N. L., Church, J. A., 2011. Observed decreases in oxygen content of the global ocean. Geophys. Res. Lett. 38.
Hewitt, H. T., Bell, M. J., Chassignet, E. P., Czaja, A., Ferreira, D., Griffies, S. M., Hyder, P., McClean, J. L., New, A. L., Roberts, M. J., 2017. Will high-resolution global ocean models benefit coupled predictions on short-range to climate timescales? Ocean Modell. 120, 120–136.
Hewitt, H. T., Fox-Kemper, B., Pearson, B., Roberts, M., Klocke, D., 2022. The small scales of the ocean may hold the key to surprises. Nat. Clim. Change 12, 496–499.
Hewitt, H. T., Roberts, M., Mathiot, P., Biastoch, A., Blockley, E., Chassignet, E. P., Fox-Kemper, B., Hyder, P., Marshall, D. P., Popova, E., Treguier, A., Zanna, L., Yool, A., Yu, Y., Beadling, R., Bell, M. J., Kuhlbrodt, T., Arsouze, T., Bellucci, A., Castruccio, F., Gan, B., Putrasahan, D., Roberts, C. D., Van Roekel, L., Zhang, Q., 2020. Resolving and parameterising the ocean mesoscale in earth system models. Curr. Clim. Change Rep. 6, 137–152.
Hofman, M., Morales Maqueda, M. A., 2011. The response of Southern Ocean eddies to increased midlatitude westerlies: A non-eddy resolving model study. Geophys. Res. Lett. 38, L03605.
Holmes, R. M., Groeskamp, S., Stewart, K., McDougall, T. J., 2022. Sensitivity of a coarse-resolution global ocean model to spatially variable neutral diffusion. J. Adv. Model. Earth Syst. 14, e2021MS002914.
IPBES, 2019. Global assessment report on biodiversity and ecosystem services of the Intergovernmental Science-Policy Platform on Biodiversity and Ecosystem Services.
IPCC, 2019. IPCC Special Report on the Ocean and Cryosphere in a Changing Climate.
Jackson, L., Hughes, C. W., Williams, R. G., 2006. Topographic control of basin and channel flows: the role of the bottom pressure torques and friction. J. Phys. Oceanogr. 36, 1786–1805.
Jansen, M. F., Adcroft, A., Khani, S., Kong, H., 2019. Toward an energetically consistent, resolution aware parameterization of ocean mesoscale eddies. J. Adv. Model. Earth Syst. 1, 1–17.
Jansen, M. F., Adcroft, A. J., Hallberg, R., Held, I. M., 2015. Parameterization of eddy fluxes based on a mesoscale energy budget. Ocean Modell. 92, 28–41.
Jones, C. S., Abernathey, R. P., 2019. Isopycnal mixing controls deep ocean ventilation. Geophys. Res. Lett. 46, 13144–13151.
Jones, C. S., Abernathey, R. P., 2021. Modeling water-mass distributions in the modern and LGM ocean: Circulation change and isopycnal and diapycnal Mixing. J. Phys. Oceanogr. 51, 1523–1538.
Khwatiwala, S., Graven, H., Payne, S., Heimbach, P., 2018. Changes to the air-sea Flux and distribution of radiocarbon in the ocean over the 21st

century,. Geophys. Res. Lett. 45, 5617–5626.
Klocker, A., Marshall, D. P., 2014. Advection of baroclinic eddies by depth mean flow. Geophys. Res. Lett. 41, L060001.
Kwiatkowski, L., Torres, O., Bopp, L., Aumont, O., Chamberlain, M., Christian, J. R., Dunne, J. P., Gehlen, M., Ilyina, T., John, J. G., Lenton, A., Li, H., Lovenduski, N. S., Orr, J. C., Palmieri, J., Santana-Falcón, Y., Schwinger, J., Séférian, R., Stock, C. A., Tagliabue, A., Takano, Y., Tjiputra, J., Toyama, K., Tsujino, H., Watanabe, M., Yamamoto, A., Yool, A., Ziehn, T., 2020. Twenty-first century ocean warming, acidification, deoxygenation, and upper-ocean nutrient and primary production decline from cmip6 model projections. Biogeosciences 17, 3439–3470.
Lee, H., Moon, B., Jung, H., Park, J., Shim, S., La, N., Kim, A., Yum, S. S., Ha, J., Byun, Y., Sung, H. M., Lee, J., 2022. Development of the UKESM-TOPAZ Earth System Model (Version 1.0) and preliminary evaluation of its biogeochemical simulations. Asia-Pac. J. Atmos. Sci. 58 (3), 379–400.
Lévy, M., Iovlino, D., Resplandy, L., Klein, P., Madec, G., Tréguier, A., Masson, S., Takahashi, K., 2012. Large-scale impacts of submesoscale dynamics on phytoplankton: Local and remote effects. Ocean Modell. 43–44, 77–93.
Lévy, M., Klein, P., Tréguier, A., Iovino, D., Madec, G., Masson, S., Takahashi, K., 2010. Modifications of gyre circulation by sub-mesoscale physics. Ocean Modell. 34, 1–15.
Lévy, M., Resplandy, L., Lengaigne, M., 2014. Oceanic mesoscale turbulence drives large biogeochemical interannual variability at middle and high latitudes. Geophys. Res. Lett. 41, 2467–2474.
Lévy, M., Visbeck, M., Naik, N., 1999. Sensitivity of primary production to different eddy parameterizations: A case study of the spring bloom development in the northwestern Mediterranean Sea. J. Mar. Res. 57 (3), 427–448.
Li, G., Cheng, L., Zhu, J., Trenberth, K. E., Mann, M. E., Abraham, J. P., 2020. Increasing ocean stratification over the past half-century. Nat. Clim. Change 10 (12), 1116–1123.
Lotze, H. K., Tittensor, D. P., Bryndum-Buchholz, A., Eddy, T. D., Cheung, W. W. L., Galbraith, E. D., Barange, M., Barrier, N., Bianchi, D., Blanchard, J. L., Bopp, L., Büchner, M., Bulman, C. M., Carozza, D. A., Christensen, V., Coll, M., Dunne, J. P., Fulton, E. A., Jennings, S., Jones, M. C., Mackinson, S., Maury, O., Niiranen, S., Oliveros-Ramos, R., Roy, T., Fernandes, J. A., Schewe, J., Shin, Y., Silva, T. A. M., Steenbeek, J., Stock, C. A., Verley, P., Volkholz, J., Walker, N. D., Worm, B., 2019. Global ensemble projections reveal trophic amplification of ocean biomass declines with climate change. Proc. Natl. Acad. Sci. USA 116 (26), 12907–12912.
Maddison, J. R., Marshall, D. P., 2013. The Eliassen–Palm flux tensor. J. Fluid Mech. 729, 69–102.
Madec, G., 2008. NEMO ocean engine. Note du Pôle de modélisation, Institut Pierre-Simon Laplace (IPSL), No. 27.
Mak, J., Avdis, A., David, T. W., Lee, H. S., Na, Y., Yan, F. E., 2022a. On constraining the mesoscale eddy energy dissipation time-scale. J. Adv. Model. Earth Syst. 14, e2022MS003223.
Mak, J., Maddison, J. R., Marshall, D. P., Munday, D. R., 2018. Implementation of a geometrically informed and energetically constrained mesoscale eddy parameterization in an ocean circulation model. J. Phys. Oceanogr. 48, 2363–2382.
Mak, J., Marshall, D. P., Maddison, J. R., Bachman, S. D., 2017. Emergent eddy saturation from an energy constrained parameterisation. Ocean Modell. 112, 125–138.
Mak, J., Marshall, D. P., Madec, G., Maddison, J. R., 2022b. Acute sensitivity of global ocean circulation and heat content to eddy energy dissipation time-scale. Geophys. Res. Lett. 49(8), e2021GL097259.
Marshall, D. P., Adcroft, A. J., 2010. Parameterization of ocean eddies: Potential vorticity mixing, energetics and Arnold's first stability theorem. Ocean Modell. 32, 1571–1578.
Marshall, D. P., Ambaum, M. H. P., Maddison, J. R., Munday, D. R., Novak, L., 2017. Eddy saturation and frictional control of the Antarctic Circumpolar Current. Geophys. Res. Lett. 44, 286–292.
Marshall, D. P., Maddison, J. R., Berloff, P. S., 2012. A framework for parameterizing eddy potential vorticity fluxes. J. Phys. Oceanogr. 42, 539–557.
Marshall, J., Adcroft, A., Hill, C., Perelman, L., Heisey, C., 1997a. A finite volume, incompressible Navier–Stokes model for studies of the ocean on parallel computers. J. Geophys. Res. 102, 5753–5766.
Marshall, J., Hill, C., Perelman, L., Adcroft, A., 1997b. Hydrostatic, quasi-hydrostatic, and non-hydrostatic ocean modelling. J. Geophys. Res. 102, 5733–5752.
Martiny, A. C., Hagstrom, G. I., DeVries, T., Letscher, R. T., Britten, G. L., Garcia, C. A., Galbraith, E., Karl, D., Levin, S. A., Lomas, M. W., Moreno, A. R., Talmy, D., Wang, W., Matsumoto, K., 2022. Marine phytoplankton resilience may moderate oligotrophic ecosystem responses and biogeochemical feedbacks to climate change. Limnol. Oceanogr. 67, S378–S389.
Matear, R. J., 2001. Effects of numerical advection schemes and eddy parameterizations on ocean ventilation and oceanic anthropogenic CO2 uptake. Ocean Modell. 3, 217–248.
Matear, R. J., Hirst, A. C., McNeil, B. I., 2000. Changes in dissolved oxygen in the Southern Ocean with climate change. Geochem. Geophys. 1 (11).
Munday, D. R., Johnson, H. L., Marshall, D. P., 2013. Eddy saturation of equilibrated circumpolar currents. J. Phys. Oceanogr. 43, 507–532.
Newsom, E., Zanna, L., Khatiwala, S., 2022. Relating patterns of added and redistributed ocean warming. J. Climate 35, 4627–4643.
Ni, Q., Zhai, X., Wang, G., Hughes, C. W., 2020a. Widespread mesoscale dipoles in the global ocean. J. Geophys. Res. Oceans 125, e2020JC016479.
Ni, Q., Zhai, X., Wang, G., Marshall, D. P., 2020b. Random movement of mesoscale eddies in the global ocean. J. Phys. Oceanogr. 50, 2341–2357.
Poulsen, M. B., Jochum, M., Maddison, J. R., Marshall, D. P., Nuterman, R., 2019. A geometric interpretation of Southern Ocean eddy form stress. J. Phys. Oceanogr. 49, 2553–2570.
Pradal, M., Gnanadesikan, A., 2014. How does the Redi parameter for mesoscale mixing impact global climate in an Earth system model? J. Adv. Model. Earth Syst. 6, 586–601.
Rahmstorf, S., 2002. Ocean circulation and climate during the past 120,000 years. Nature 419, 207–214.
Redi, M. H., 1982. Oceanic isopycnal mixing by coordinate rotation. J. Phys. Oceanogr. 12, 1154–1158.
Roberts, M. J., Jackson, L. C., Roberts, C. D., Meccia, V., Docquier, D., Koenigk, T., Ortega, P., Moreno-Chamarro, E., Bellucci, A., Coward, A. C., Drijfhout, S., Exarchou, E., Gutjahr, O., Hewitt, H., Iovino, D., Lohmann, K., Putrasahan, D., Schiemann, R., Seddon, J., Terray, L., Xu, X., Zhang, Q., Chang, P., Yeager, S. G., Castruccio, F. S., Zhang, S., Wu, L., 2020. Sensitivity of the Atlantic Meridional Overturning Circulation

to model resolution in CMIP6 HighResMIP simulations and implications for future changes. J. Adv. Model. Earth Sys. 12, e2019MS002014.
Sarmiento, J. L., Gruber, N., 2006. Ocean Biogeochemical Dynamics. Princeton University Press.
Séférian, R., Nabat, P., Michou, M., Saint-Martin, D., Voldoire, A., Colin, J., Decharme, B., Delire, C., Berthet, S., Chevallier, M., Sénési, S., Franchisteguy, L., Vial, J., Mallet, M., Joetzjer, E., Geoffroy, O., Guérémy, J., Moine, M., Msadek, R., Ribes, A., Rocher, M., Roehrig, R., Salas-y-Mélia, D., Sanchez, E., Terray, L., Valcke, S., Waldman, R., Aumont, O., Bopp, L., Deshayes, J., Éthé, C., Madec, G., 2019. Evaluation of CNRM Earth System Model, CNRM-ESM2-1: Role of Earth system processes in present-day and future climate. J. Adv. Model. Earth. Syst. 11 (12), 4182–4227.
Sérazin, G., Jaymond, A., Leroux, S., Penduff, T., Bessières, L., Llovel, W., Barnier, B., Molines, J., Terray, L., 2017. A global probabilistic study of the ocean heat content low-frequency variability: Atmospheric forcing versus oceanic chaos. Geophys. Res. Lett. 44 (11), 5580–5589.
Smith, K. S., Marshall, J., 2009. Evidence for enhanced eddy mixing at middepth in the Southern Ocean. J. Phys. Oceanogr. 39, 50–69.
Stewart, A. L., McWilliams, J. C., Solodoch, A., 2021. On the role of bottom pressure torques in wind-driven gyres. J. Phys. Oceanogr. 51, 1441–1464.
Swearer, S. E., Treml, E. A., Shima, J. S., 2019. A review of biophysical models of marine larval dispersal. CRC Press.
Tagliabue, A., Kwiatkowski, L., Bopp, L., Butenschön, M., Cheung, W., Lengaigne, M., Vialard, J., 2021. Persistent uncertainties in ocean net primary production climate change projections at regional scales raise challenges for assessing impacts on ecosystem services. Front. Clim. 3, 738224.
Takano, Y., Ito, T., Deutsch, C., 2018. Projected centennial oxygen trends and their attribution to distinct ocean climate forcings. Global Biogeochem. Cycles 32, 1329–1349.
Tokarska, K. B., Stolpe, M. B., Sippel, S., Fischer, E. M., Smith, C. J., Lehner, F., Knutti, R., 2020. Past warming trend constrains future warming in CMIP6 models. Sci. Adv. 6, eaaz9549.
Treguier, A. M., Held, I. M., Larichev, V. D., 1997. Parameterization of quasigeostrophic eddies in primitive equation ocean models. J. Phys. Oceanogr. 27, 567–580.
Tschumi, T., Joos, F., Gehlen, M., Heinze, C., 2011. Deep ocean ventilation, carbon isotopes, marine sedimentation and the deglacial CO_2 rise. Clim. Past. 7 (3), 771–800.
Vallis, G. K., 2006. Atmospheric and Oceanic Fluid Dynamics. Cambridge University Press.
Villani, C., 2008. Optimal Transport: Old and New. Springer.
Visbeck, M., Marshall, J., Haine, T., Spall, M., 1997. Specification of eddy transfer coefficients in coarse-resolution ocean circulation models. J. Phys. Oceanogr. 27, 381–402.
Wang, Q., Danilov, S., Sidorenko, D., Timmermann, R., Wekerle, C., Wang, X., Jung, T., Schröter, J. G., 2014. The Finite Element Sea Ice-Ocean Model (FESOM) v.1.4: formulation of an ocean general circulation model. Geosci. Model Dev. 7, 663–693.
Wang, Y., Stewart, A. L., 2020. Scalings for eddy buoyancy transfer across continental slopes under retrograde winds. Ocean Modell. 147, 101579.
Waterman, S., Hogg, N. G., Jayne, S. R., 2011. Eddy-mean flow interaction in the Kuroshio extension region. J. Phys. Oceanogr. 41, 1182–1208.
Waterman, S., Hoskins, B. J., 2013. Eddy shape, orientation, propagation, and mean flow feedback in western boundary current jets. J. Phys. Oceanogr. 43, 1666–1690.
Waterman, S., Jayne, S. R., 2012. Eddy-driven recirculations from a localized transient forcing. J. Phys. Oceanogr. 42, 430–447.
Waterman, S., Lilly, J. M., 2015. Geometric decomposition of eddy feedbacks in barotropic systems. J. Phys. Oceanogr. 45, 1009–1024.
Wei, H., Wang, Y., Stewart, A. L., Mak, J., 2022. Scalings for eddy buoyancy fluxes across prograde shelf/slope fronts. J. Adv. Model. Earth. Syst. 14, e2022MS003229.
Whitt, D. B., Jansen, M. F., 2020. Slower nutrient stream suppresses Subarctic Atlantic Ocean biological productivity in global warming. Proc. Natl. Acad. Sci. USA 117, 15504–15510.
Williams, R. G., Follows, M. J., 2011. Ocean Dynamics and the Carbon Cycle: Principles and Mechanisms. Cambridge University Press.
Williams, R. G., McDonagh, E., Roussenov, V. M., Torres-Valdes, S., Kind, B., Sanders, R., Hansell, D. A., 2011. Nutrient streams in the North Atlantic: Advective pathways of inorganic and dissolved organic nutrients. Global Biogeochem. Cycles 25, GB4008.
Williams, R. G., Roussenov, V. M., Follows, M. J., 2017. Nutrient streams and their induction into the mixed layer. Global Biogeochem. Cycles 20, GB1016.
Zanna, L., Brankart, J. M., Huber, M., Leroux, S., Penduff, T., Williams, P. D., 2019a. Uncertainty and scale interactions in ocean ensembles: From seasonal forecasts to multidecadal climate predictions. Q. J. Roy. Met. Soc. 145 (S1), 160–175.
Zanna, L., Khatiwala, S., Gregory, J. M., Ison, J., Heimbach, P., 2019b. Global reconstruction of historical ocean heat storage and transport. Proc. Natl. Acad. Sci. USA 116, 1126–1131.
Zhang, Y., Vallis, G. K., 2013. Ocean heat uptake in eddying and non-eddying ocean circulation models in a warming climate. J. Phys. Oceanogr. 43, 2211–2229.